

Ludwig-Maximilians-Universität München

Sektion Physik

**Search for Single Top Quark Production
at LEP2 in the Leptonic W Boson Decay
Channel**

Diplomarbeit

von

Meta Binder

30. April 2001

Ludwig-Maximilians-Universität München

Sektion Physik

**Search for Single Top Quark Production
at LEP2 in the Leptonic W Boson Decay
Channel**

Diplomarbeit

von

Meta Binder

30. April 2001

Erstgutachterin: Prof. Dr. D. Schaile
Zweitgutachter: Prof. Dr. W. Blum

”Es ist nicht das Wissen, sondern das Lernen,
nicht das Besitzen, sondern das Erwerben,
nicht das Da-sein, sondern das Hinkommen,
was den größten Genuss gewährt.”

Carl-Friedrich Gauss (geb. 30.04.1777)

Für meine Eltern
Katharina und Michael

Contents

1	Introduction	3
2	Theoretical Background	5
2.1	Standard Model	5
2.1.1	Quarks, Leptons and Gauge Bosons	5
2.1.2	Electroweak Unification	6
2.2	Top-Charm Associated Production in the Standard Model	7
2.3	FCNC Beyond the Standard Model	9
2.4	Flavor Changing Neutral Current Processes at LEP2	10
2.5	The Leptonic Decay Channel	12
3	Experiment Overview	15
3.1	The Large Electron Positron Collider (LEP)	15
3.2	The OPAL Detector	17
3.2.1	The Central Detector	18
3.2.2	The Time-of-Flight Detector (TOF),	19
3.2.3	The Calorimeter System	19
3.2.4	The Muon System	20
3.2.5	The Forward Detector and the SiW Luminometer	20
3.2.6	The Trigger and Data Acquisition	20
4	Data and Monte Carlo Samples	21
4.1	Data Samples	21
4.2	Monte Carlo Samples	22
4.2.1	Signal	22
4.2.2	Background	22
5	Single Top Quark Analysis	23
5.1	Event Selection	23
5.1.1	Global Event Selection	23
5.1.2	Lepton Identification	24
5.1.3	Jet finding	24
5.1.4	b-Tagging	24
5.2	Motivation for Preselection Cuts and Likelihood	25
5.3	Preselection for Single Top Candidates	27
5.4	Likelihood Selection	33

6 Results	39
6.1 Limit on the cross section	39
6.2 Uncertainties of the limit from the top quark mass	41
6.3 The limit for the anomalous coupling constants	41
7 Summary and Conclusions	43
A Cut-based Study for Single Top Quark Production	45
Bibliography	50

Chapter 1

Introduction

The discovery of the top quark at the $p\bar{p}$ collider Tevatron in the year 1995 [1] not only justified the existence of the b quark partner in the third generation of quarks of the Standard Model but opened new possibilities for experimental research beyond it. The properties of the top quark could reveal information on flavor physics. The search for flavor changing neutral current (FCNC) decays is of special interest. The absence of FCNCs at low energy does not necessarily forbid large FCNCs at high mass scales [2]. The present thesis performs a search for single top quark production via these FCNC interactions.

In the Standard Model framework flavor violating transitions only arise through 'loops' and are highly suppressed due to the unitarity of the Cabbibo-Kobayashi-Maskawa Matrix [3] and a strong Glashow-Ilioupoulos-Maiani [4] suppression. As a result the cross section of these transitions is very small.

Contributions to FCNC interactions from extensions of the Standard Model i.e. supersymmetric models, two or multiple Higgs doublet models or in exotic models such as compositeness can be up to 5 orders of magnitude larger than their Standard Model counterparts. Therefore the FCNC interactions for single top production offer an ideal place to search for new physics beyond the Standard Model. The FCNC vertices $t\bar{c}(u)V$ ($V = \gamma, Z$) can be probed either in rare decays of the top quark or via top-charm associated production. The latter is studied in the present thesis. A brief introduction to flavor violating interactions within and beyond the Standard Model is presented in Chapter 2.

The search for FCNC processes is of special interest at high energy colliders, in particular e^+e^- colliders, due to the clean environment that they offer. The investigated data was collected by the OPAL detector at the Large Electron-Positron Collider (LEP), which has been situated at the European Laboratory for Particle Physics near Geneva. When produced via FCNC in a two body reaction $e^+e^- \rightarrow t\bar{c}(\bar{t}c)$ at the energies of LEP2, the top quark [5] ($m_{\text{top}} = 174.3 \pm 5.1 \text{ GeV}^1$) takes up energies greater than the half of the total energy leading to a highly distinctive kinematical signature. At such energy the detection of a top quark would clearly indicate that it is singly produced. A brief description of the LEP collider and the OPAL detector is given in Chapter 3.

A full detector response simulation is available to create Monte Carlo samples for the expected signal and the Standard Model background, which subsequently are com-

¹Throughout this thesis c and \hbar are set to unity: $c=1=\hbar$

pared to the data samples. Therefore an excess in the data compared to the Standard Model background, would signal new physics. The description of the used samples is given in Chapter 4.

The full analysis of the data is elaborated in Chapter 5. The present analysis concentrates on the leptonic W boson decay originating from the single top quark decay and is referred to as leptonic channel.

Two approaches are followed in the present analysis: a cut-based and a likelihood selection method. The latter is used and performed for two data samples recorded at center-of-mass energies of $\sqrt{s} = 189$ GeV and $\sqrt{s} = 206$ GeV. A cut-based study using the data at $\sqrt{s} = 189$ GeV is presented in Appendix A.

The signal events are known to have the following topology: two jets (originating from a charm and beauty quark), one isolated lepton and a large missing transverse momentum from a neutrino. This kinematic topology is used to select a set of cuts, which reduce the background while retaining the signal. Events passing this preselection enter the likelihood method. An efficient b-tag algorithm is used to separate the signal from the main background and a neural network locates the isolated leptons.

The largest systematic uncertainty on the cross section comes from the top quark mass uncertainty. This is taken into account by using samples of signal Monte Carlos at three different top quark masses. The final results for single top quark production via FCNC are evaluated in Chapter 6. A model independent limit on the signal cross section for both center-of-mass energies $\sqrt{s} = 189$ GeV and $\sqrt{s} = 206$ GeV is deduced. Constraints on model dependent anomalous coupling constants for the combined data are derived and compared to the results obtained by other LEP experiments.

Chapter 2

Theoretical Background

In this chapter a brief introduction to the Standard Model [6, 7, 8] is given, with emphasis on the electroweak interaction. Single top quark production within and beyond the Standard Model is discussed. The search for flavor changing neutral currents (FCNC) at LEP2 is motivated.

2.1 Standard Model

The Standard Model (SM) of elementary particle physics enfoldes the unified theory of the electroweak interaction and the quantum chromodynamics (QCD) [9].

2.1.1 Quarks, Leptons and Gauge Bosons

The elementary particles of the SM are the quarks, the leptons and the gauge bosons. Quarks and leptons fall into three 'families' or 'generations'. The numbering of the generations is ascending with the mass of the particles. All fermions (spin 1/2) - lep-

fermions	family	electric charge	spin
	1 2 3		
leptons	ν_e ν_μ ν_τ	0	1/2
	e μ τ	-1	1/2
quarks	u c t	+2/3	1/2
	d s b	-1/3	1/2

Table 2.1: Quarks and leptons of Standard Model.

tons and quarks - have antifermions with the same mass, but opposite electric charge [10]. There are three elementary interactions next to gravitation, each being negotiated by gauge bosons (spin 1): eight massless gluons (g), which are mediators for the strong interaction, one massless photon (γ), which is the mediator of the electromagnetic interaction and three massive gauge bosons (W^+ , W^- , Z^0), which are mediators for the weak interaction. The leptons interact via the weak force and if charged additionally via the electromagnetic force. The quarks are subject to all interactions [9].

2.1.2 Electroweak Unification

The electromagnetic and weak interaction are unified in a theory, where they appear as different manifestations of one fundamental 'electroweak' interaction (Glashow-Weinberg-Salam (GWS) theory). The underlying symmetry group is called $SU(2)_L \times U(1)$. $SU(2)_L$ refers to the weak isospin (with a subscript to remind that it involves left-handed¹ states only) and $U(1)$ refers to the weak hypercharge [9]. Quarks involved in the weak interaction processes are related to the physical quarks through the Cabibbo-Kobayashi-Maskawa (CKM) matrix defined as follows:

$$\begin{pmatrix} d' \\ s' \\ b' \end{pmatrix} = \begin{pmatrix} U_{ud} & U_{us} & U_{ub} \\ U_{cd} & U_{cs} & U_{cb} \\ U_{td} & U_{ts} & U_{tb} \end{pmatrix} \begin{pmatrix} d \\ s \\ b \end{pmatrix}$$

The quarks d' , s' and b' emerge by Cabibbo-rotation from the mass-eigenstates. The CKM matrix expresses possible mixing between quarks in the same family as well as between different families [9].

The left-handed leptons (right-handed antileptons) and the (Cabibbo-rotated) left-

	fermion multiplets	I	I ₃
leptons	$\begin{pmatrix} \nu_e \\ e \end{pmatrix}_L$	1/2	+1/2
	$\begin{pmatrix} \nu_\mu \\ \mu \end{pmatrix}_L$		-1/2
	$\begin{pmatrix} \nu_\tau \\ \tau \end{pmatrix}_L$	0	0
quarks	$\begin{pmatrix} u \\ d' \end{pmatrix}_L$	1/2	+1/2
	$\begin{pmatrix} c \\ s' \end{pmatrix}_L$		-1/2
	$\begin{pmatrix} t \\ b' \end{pmatrix}_L$	0	0
	u_R	0	0
	c_R	0	0
	t_R	0	0
	d_R	0	0
	s_R	0	0
	b_R	0	0

Table 2.2: Multiplets of the electroweak interaction. All antiparticles have opposite handedness but the same isospin (I, I₃).

handed quarks (right-handed antiquarks) from each family form doublets (Table 2.2), which can transform into each other by emission or absorption of W bosons. A full 'weak isospin' symmetry is contemplated for these particles. They are assigned to have a weak isospin $I = 1/2$ and its third component to be $I_3 = \pm 1/2$.

Right-handed fermions (and left-handed antifermions) do not couple to W bosons. Therefore they are described as singlets ($I = I_3 = 0$).

Electro-Weak Mixing

An isotriplet of three intermediate vector bosons (W^+ , W^- , W^0) couples with the strength g_W to the fermion doublets. An isosinglet intermediate vector boson B^0 couples with strength g' to the fermions. The underlying $SU(2)_L \times U(1)$ symmetry is broken in GWS theory. The linear combination of the two neutral states, W^0 and B^0 ,

¹A particle of spin $\frac{1}{2}$ can have a helicity of +1 (spin and velocity are parallel) or -1 (spin and velocity are antiparallel). The former is called 'right-handed' and the 'latter' left-handed [9].

produces one massless combination (the photon) and a massive combination orthogonal to the photon (the Z^0) [9, 10]:

$$\begin{aligned} |\gamma\rangle &= \cos\theta_W|B^0\rangle + \sin\theta_W|W^0\rangle \\ |Z^0\rangle &= -\sin\theta_W|B^0\rangle + \cos\theta_W|W^0\rangle \end{aligned} \quad (2.1)$$

where θ_W is the weak mixing angle (also called Weinberg angle).

One of the essential ingredients of the Standard Model of leptons and quarks is the flavor diagonal structure of the electroweak neutral current, i.e. the absence of flavor-violating terms like $t \rightarrow c$. It follows as an algebraic consequence of the $SU(2)$ doublet structure of the left-handed leptons and quarks [11].

2.2 Top-Charm Associated Production in the Standard Model

As a consequence of the neutral current structure, any FCNC process within the SM is forbidden at tree-level. That is the FCNC process can only arise at higher orders through loops, due to the CKM mixing of the quarks. The process (2.2)²

$$e^+e^- \rightarrow t\bar{c}(\bar{u}). \quad (2.2)$$

is referred to as single top quark production. The total cross section at loop-level as a function of the center-of-mass energy \sqrt{s} is shown in Figure 2.1.

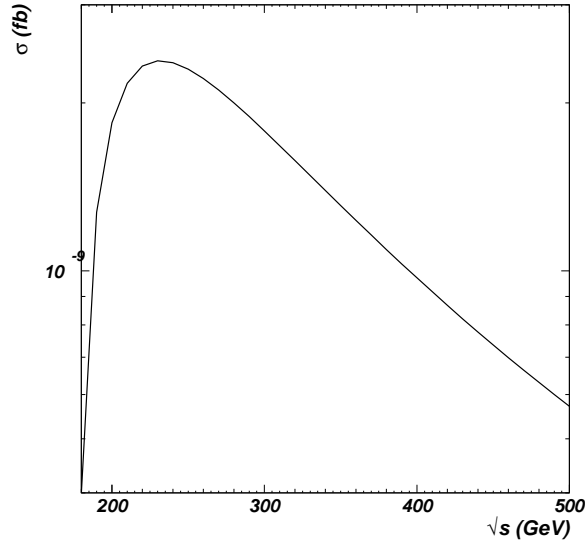


Figure 2.1: The total cross section of the process $e^+e^- \rightarrow t\bar{c}$ in the Standard Model as a function of the center-of-mass energy \sqrt{s} [12].

Carrying out calculations in the Feynman-t'Hooft gauge, the total cross section is found to be in the order of $10^{-10} - 10^{-9}$ fb and decreases when the center-of-mass

²Throughout the present thesis conjugate processes are implicit.

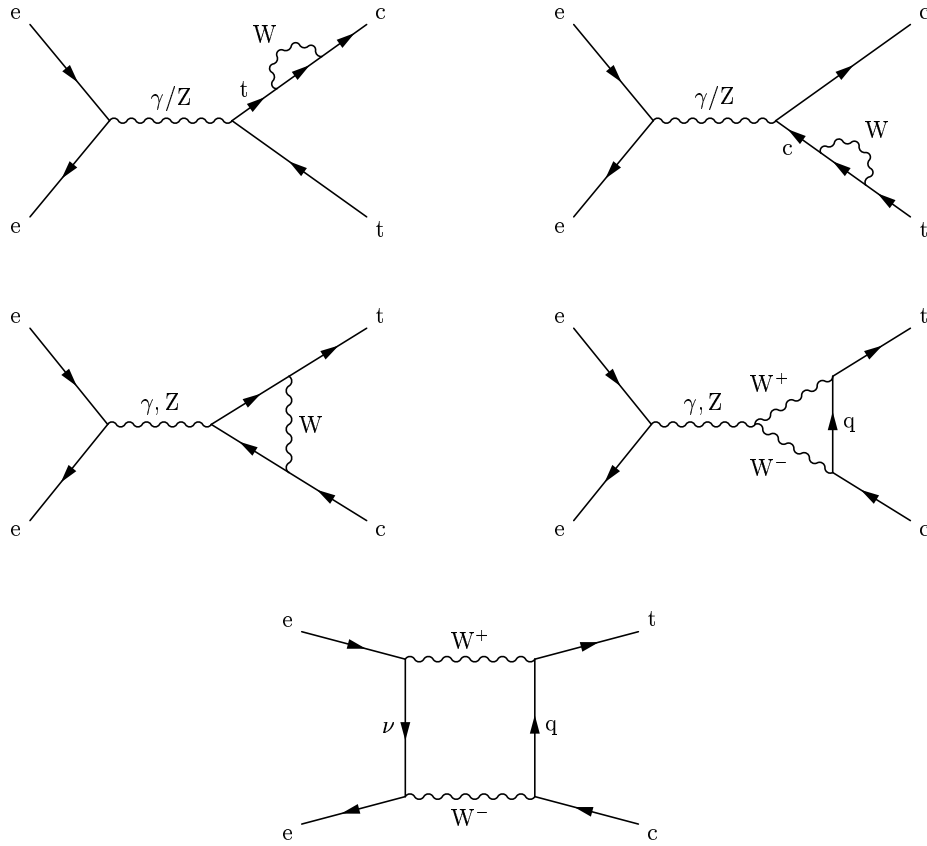


Figure 2.2: The Feynman diagrams of the FCNC process $e^+e^- \rightarrow t\bar{c}$ in the Standard Model: top row self-energy, middle row triangle and the lowest plot box diagram.

energy increases beyond ≥ 250 GeV. The cross section for the process (2.2) at LEP2 center-of-mass energy $\sqrt{s} = 200$ GeV is [12]

$$\sigma(e^+e^- \rightarrow t\bar{c}) = 1.84 \times 10^{-9} \text{ fb} . \quad (2.3)$$

It is too small to be of experimental relevance as the total recorded amount of integrated luminosity is too small ($\sim 200 \text{ pb}^{-1}$). In models beyond the SM new particles may appear in the loop and would give significant contributions to flavor changing transitions.

There are three kinds of Feynman diagrams at one loop-level for the process (2.2) within the Standard Model [12]: 'self-energy', triangle and box diagram³ shown in Figure 2.2. The contributions from neutral Higgs and Goldstone bosons are neglected.

Another process within the SM for single top quark production with a different final state as the one investigated is $e^+e^- \rightarrow e^-\bar{\nu}_e t\bar{b}$. At $\sqrt{s} = 200$ GeV the cross section is in the order of [13] $\sigma(e^+e^- \rightarrow e^-\bar{\nu}_e t\bar{b}) \sim 10^{-4} \text{ fb}$, which is also not large enough for experimental observation.

³Throughout the present thesis only the c quark is mentioned, nevertheless every reference to the c quark also applies for the u quark.

2.3 FCNC Beyond the Standard Model

The cross section for single top quark production within the Standard Model is very small. As a consequence any observation of FCNC couplings deviating from SM expectations will unambiguously signal the presence of new physics. Extensions of the Standard Model could lead to measurable effects for FCNC single top quark production.

In the following, three models for possible top quark production and decay are briefly introduced:

1. General arguments, based on hierarchical and democratic symmetries are used to derive anomalous vertices for the production of single top quarks via FCNC in e^+e^- annihilations. A total cross section for $e^+e^- \rightarrow (\gamma, Z) \rightarrow \bar{c}t$ has been derived which yields a numerical value of [14]

$$\sigma(e^+e^- \rightarrow \bar{c}t) = 6.3 \cdot 10^{-2} \text{ pb}, \quad \sqrt{s} = 190 \text{ GeV} \quad (2.4)$$

for a branching ratio of $\text{BR}(t \rightarrow c\gamma) = \text{BR}(t \rightarrow cZ) = 1\%$ with respect to $\Gamma(t \rightarrow bW)$.

2. The process $t \rightarrow cV$, ($V = \gamma, Z$) can be examined in two-Higgs doublet models. Two distinct models are considered. In the first model one doublet gives the masses to all fermions and the other doublet essentially decouples from the fermions. In the second model one doublet gives mass to the up-type quarks, while the down-type quarks and charged leptons receive a mass from the other doublet.

Large enhancements of the SM branching fractions $\text{BR}_{\text{SM}}(t \rightarrow c\gamma, cZ) \sim 10^{-12}$ are possible for the most optimistic values, giving the overall maximum values of branching fractions to be [15]

$$\text{BR}(t \rightarrow c\gamma, cZ) \sim 10^{-8} - 10^{-9}. \quad (2.5)$$

for both models mentioned above.

3. Rare electroweak-like one-loop supersymmetric contributions and flavor violating decays of the top quark into a charm quark and a gauge boson are calculated in the framework of low-energy supersymmetry. For the most optimistic values, the following branching ratios with respect to $\Gamma(t \rightarrow bW)$ were found [16]:

$$\text{BR}(t \rightarrow c\gamma, cZ) \sim 10^{-8} - 10^{-6}. \quad (2.6)$$

The branching fractions given above enhance the Standard Model predictions by 5 orders of magnitude or even higher if one looks at the predictions given in Equation (2.4) for single top quark production at LEP2.

2.4 Flavor Changing Neutral Current Processes at LEP2

Since the summer of 1997, the LEP collider operated at energies greater or equal to $\sqrt{s} \geq 184$ GeV. At this total center-of-mass energy the production of single top quarks via FCNC is kinematically possible:

$$e^+e^- \rightarrow Z(\gamma) \rightarrow t\bar{c} \quad (2.7)$$

The Feynman diagram of this non Standard Model process (2.7) at tree-level is shown in Figure 2.3, where the 'bubble' describes the ignorance of the FCNC vertex.

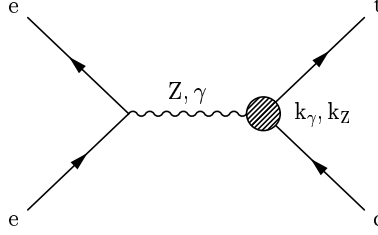


Figure 2.3: The Feynman diagram of the FCNC transition. The anomalous coupling constants k_γ and k_Z for the γ and Z boson exchange are indicated.

A parameterization of FCNC transitions in terms of model independent anomalous coupling constants k_γ and k_Z [17] is also indicated and corresponds to the annihilation via the photon and the Z boson, respectively.

Phenomenological limits on FCNC branching ratios for the top quark decays have been derived by the CDF collaboration in $p\bar{p}$ collisions [18]:

$$\begin{aligned} \text{BR}(t \rightarrow c(u)\gamma) &< 3.2\% \quad (95\% \text{ C.L.}) \\ \text{BR}(t \rightarrow c(u)Z) &< 33\% \quad (95\% \text{ C.L.}) \end{aligned} \quad (2.8)$$

The vertices of the FCNC interactions $\gamma \rightarrow t\bar{c}$ and $Z \rightarrow t\bar{c}$ can be written as follows⁴ [17]:

$$\begin{aligned} \Gamma_\mu^\gamma &= k_\gamma \frac{ee_q}{\Lambda} \sigma_{\mu\nu} \\ \Gamma_\mu^Z &= k_Z \frac{e}{\sin(2\theta_W)} \gamma_\mu \end{aligned} \quad (2.9)$$

where Λ is a scale parameter describing the energy scale of the underlying dynamics (set to the top quark mass), k_γ and k_Z define the values for the strength of the anomalous couplings, which are constraint by the CDF limits (Eq: (2.8)) to $k_\gamma^2 < 0.176$ and $k_Z^2 < 0.533$. In the following it is assumed that k_γ and k_Z are positive and real and $\Lambda = m_t$.

The total cross section for single top quark production via FCNC for the process (2.7)

⁴ e is the electric charge, $e_q = 2/3$ is the charge of the top quark, θ_W is the Weinberg angle and $\sigma^{\mu\nu} = \frac{1}{2}(\gamma^\mu \gamma^\nu - \gamma^\nu \gamma^\mu)$.

at the Born level is then given by [17]:

$$\sigma(e^+e^- \rightarrow t\bar{c}) = \frac{\pi\alpha^2}{s} \left(1 - \frac{m_t^2}{s}\right)^2 \left[k_\gamma^2 e_q^2 \frac{s}{m_t^2} \left(1 + \frac{2m_t^2}{s}\right) + \frac{(1 + a_w^2) \left(2 + \frac{m_t^2}{s}\right)}{4\sin^4 2\theta_W \left(1 - \frac{m_Z^2}{s}\right)^2} + 3k_\gamma k_Z \left(\frac{m_t}{\Lambda}\right) \frac{a_w e_q}{\sin^2 2\theta_W \left(1 - \frac{m_Z^2}{s}\right)} \right] \quad (2.10)$$

where α is the fine structure constant, s is the center-of-mass energy squared, m_t is the mass of the top quark, m_Z is the Z boson mass and $a_w = 1 - 4\sin^2\theta_W$. The mass of the associated light quark is assumed to be zero ($m_c = 0$). The three terms in equation (2.10) correspond to the γ exchange ($\sim k_\gamma^2$), the Z boson exchange ($\sim k_Z^2$) and the $\gamma - Z$ interference ($\sim k_\gamma k_Z$), respectively. Corrections due to the finite widths of the top quark and W boson are negligible at LEP2 energies.

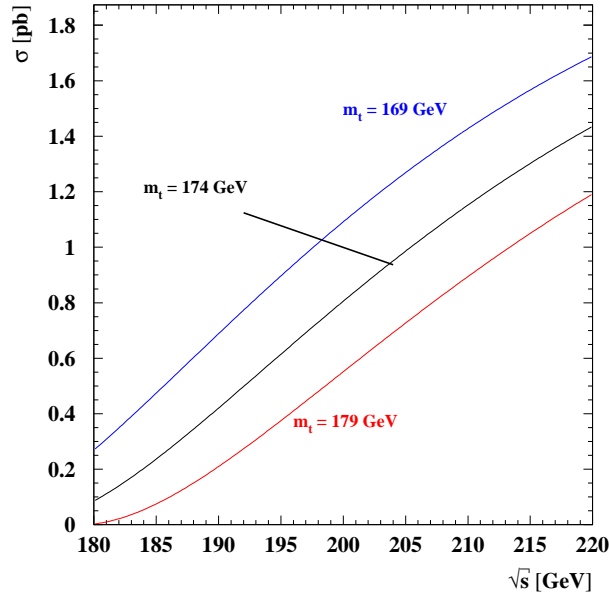


Figure 2.4: The cross section for $e^+e^- \rightarrow t\bar{c}(\bar{u})$ as a function of \sqrt{s} . Three different top quark masses are considered: $m_t = 169, 174$ and 179 GeV for k_γ, k_Z derived from the CDF limits.

The estimates of the total cross section for the process (2.7) is shown in Figure 2.4 as a function of the center-of-mass energy \sqrt{s} . The cross section is calculated with $m_t = 169, 174$ and 179 GeV using the anomalous coupling constants k_γ, k_Z derived from the CDF limits (Eq: (2.8)). The dominating contribution to the cross section comes from the Z boson exchange [17]:

$$\sigma(e^+e^- \rightarrow \gamma) \propto \left(1 - \frac{m_t^2}{s}\right)^2, \quad \sigma(e^+e^- \rightarrow Z) \propto \frac{1}{s} \left(1 - \frac{m_t^2}{s}\right)^2$$

The cross section (2.10) shows a typical threshold character. Therefore the limits on k_γ, k_Z are very sensitive on the top mass.

At the center-of-mass-energies of LEP2 the top quark would be produced very close to its threshold production. Due to this fact, there is a distinctive 'kinematical' final state signature for the FCNC single top quark production: there are practically fixed values for the energies of the final jets and the W boson. The Feynman diagram for this process is shown in Figure 2.5.

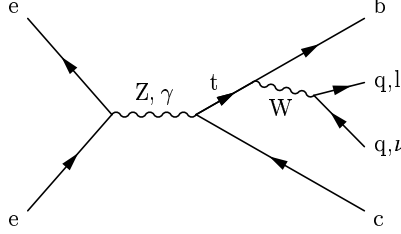


Figure 2.5: Feynman diagram of the FCNC single top quark production: $e^+e^- \rightarrow t\bar{c} \rightarrow bW\bar{c}$; $q = \text{quark}, l = \text{lepton}$ and $\nu = \text{neutrino}$.

The top quark is produced almost at rest ($E_t \approx m_t$) and the accompanying light quark has a small energy:

$$E_c \simeq \frac{s - m_t^2 + m_c^2}{2\sqrt{s}} \simeq \sqrt{s} - m_t \quad (2.11)$$

The width of the top quark $\Gamma \approx 1.5 \text{ GeV}$ is much larger than the typical hadronisation scale $\Lambda_{\text{QCD}} \approx 208 \text{ MeV}$ [5]. Therefore the top quark decays before hadronisation effects set in. This fact leads to a suppression of nonperturbative effects in top quark production and decay.

The beauty quark and the W boson from the top decay have energies given by following expressions [17]:

$$E_b \simeq \frac{m_t^2 - m_W^2 + m_b^2}{2m_t} \quad (2.12)$$

$$E_W \simeq \frac{m_t^2 + m_W^2 - m_b^2}{2m_t} \quad (2.13)$$

The corresponding distributions as a function of the energy of the final particles are shown in Figure 2.6. The energy distribution of the jets is determined only by the kinematics of the $t\bar{c}$ process and very weakly depends on the parameters of the model for FCNC interaction.

2.5 The Leptonic Decay Channel

The W boson produced in a FCNC process (Fig: 2.5) decays hadronically via $W \rightarrow q\bar{q}$ and leptonically via $W \rightarrow l\bar{\nu}$. The branching fractions for these decays are [5]:

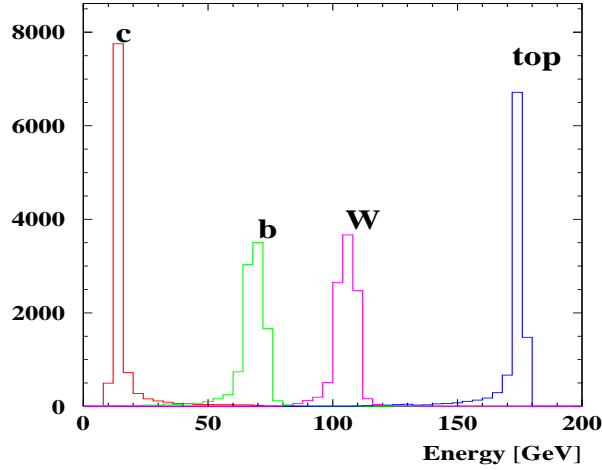


Figure 2.6: The energy distributions on parton level for the charm quark, the beauty quark, the W boson and the energy of the top quark at $\sqrt{s} = 189$ GeV.

$$\text{BR}(W \rightarrow q\bar{q}) = (68.5 \pm 0.6)\% \quad \text{BR}(W \rightarrow l\bar{\nu}) = (31.68 \pm 0.14)\%.$$

Therefore two final state signatures arise referred to as: hadronic and leptonic channel. The present analysis concentrates on the leptonic W boson decay of the single top quark production:

$$e^+e^- \rightarrow t\bar{c} \rightarrow bl\nu\bar{c} \quad (l = e, \mu, \tau) \quad (2.14)$$

The signature of single top quark events in the leptonic channel consists of:

- two jets (with large difference in energy, one is a jet originating from a beauty quark, the other from a light quark)
- one isolated high energetic lepton
- large missing transverse momentum from the neutrino

The invariant mass from the lepton and neutrino must equal the W boson mass, since they are products of its decay.

The limits given by the CDF collaboration only weakly constrain the FCNC branching fractions (Eq: (2.8)). Nevertheless the three-generation unitarity of the CKM-Matrix implies that U_{tb} must be near unity [19]. Therefore only the top decay $t \rightarrow bW$ is investigated in the present analysis. In a pessimistic scenario the efficiencies should be rescaled by 64%.

The full analysis of this channel is elaborated in Chapter 5. Monte Carlo samples simulating the signal (Eq: (2.14)) and the expected background from Standard Model sources are compared to the data samples (see Chapter 4) in order to get an efficient separation between the signal from the background.

Chapter 3

Experiment Overview

The accelerator at the European Laboratory for Particle Physics (CERN) in Geneva / Switzerland and one of its four detectors - OPAL - are discussed briefly in this chapter. A detailed description of the OPAL detector can be found in [20].

3.1 The Large Electron Positron Collider (LEP)



Figure 3.1: Aerial view of the Large Electron-Positron Collider (LEP)

The Large Electron Positron Collider (LEP) at CERN used to be the largest accelerator in the world till the recent end of its operation. In this ring - 27 km in circumference, 100 m below ground - bunches of electrons and positrons are accelerated in opposite

directions to almost the speed of light. At four points in the ring, the bunches of particles are focused down to dimensions of $200 \mu\text{m} \times 8 \mu\text{m}$ and a length of 1 cm per bunch and made to collide at the four LEP experiments, ALEPH, DELPHI, L3 and OPAL. Figure 3.1 shows an aerial view of the CERN research area, the LEP accelerator and the sites of the experiments.

The advantage of e^+e^- accelerators is the missing inner structure of the primary interacting particles. The initial state of the reaction is thus known, simplifying precision measurements. The whole center-of-mass energy, two times the beam energy, is available in the colliding particles.

A disadvantage of e^+e^- accelerators is the energy loss of electrons and positrons through synchrotron radiation when forced on a circular path. The energy loss is restored to the beam per revolution (over 11200 cycles per second) by high frequency resonator cavities. For relativistic electrons and positrons of energy E , the energy loss in a circular trajectory of radius R is given by

$$\Delta E [\text{GeV}] = 8.85 \cdot 10^{-8} \frac{E^4 [\text{GeV}^4]}{R [\text{km}]} \quad (3.1)$$

If the beam energy is 100 GeV the energy loss in the LEP ring is about 2 GeV (2% of the total energy) per circle. The radius of the accelerator and the technical design of the high frequency resonator cavities limit the maximum achievable center-of-mass energy for the LEP ring to an upper limit of 210 GeV.

One important parameter of accelerators is their luminosity \mathcal{L} , which determines the event rate dN/dt as a function of the cross section $\sigma(s)$ of an event (\sqrt{s} is the center-of-mass energy) as

$$\frac{dN}{dt} = \mathcal{L} \cdot \sigma(s) \quad (3.2)$$

The luminosity \mathcal{L} for e^+e^- storage rings is defined by the number of bunches n forming the colliding beams, the number of electrons (positrons) per bunch N_{e^-} (N_{e^+}), the horizontal and vertical bunch cross section σ_x^* and σ_y^* at the interaction point and the revolution frequency f , in the following way

$$\mathcal{L} = \frac{nN_{e^-}N_{e^+}f}{4\pi\sigma_x^*\sigma_y^*} \quad (3.3)$$

From its start in the year 1989 up to 1995 the LEP accelerators was running at a center-of-mass energy of $\sqrt{s} \approx 91 \text{ GeV}$ close to the Z^0 resonance. A precise measurement of the properties of the Z^0 boson had been carried out.

In the year 1996, the so called LEP2 period started with a center-of-mass energy of $\sqrt{s} \approx 161 \text{ GeV}$, reaching $\sqrt{s} \approx 210 \text{ GeV}$ at the final stage in the year 2000.

At this center-of-mass energy, the W boson pair production research was possible as well as the search for new physics, e.g. for the Higgs boson and particles predicted by extensions of the Standard Model.

On the 2nd November 2000 the operation of LEP was terminated. The accelerator and its experiments were dismantled to make way for the construction of the next generation accelerator, the Large Hadron Collider (LHC) - a pp collider - which will reach a center-of-mass energy of 14 TeV.

3.2 The OPAL Detector

The OPAL detector (Omni Purpose Apparatus at LEP) is one of the four experiments at the Large Electron Positron Collider in Geneva, Switzerland. It is designed to provide precise measurements of the momentum and the energy for all types of e^+e^- events.

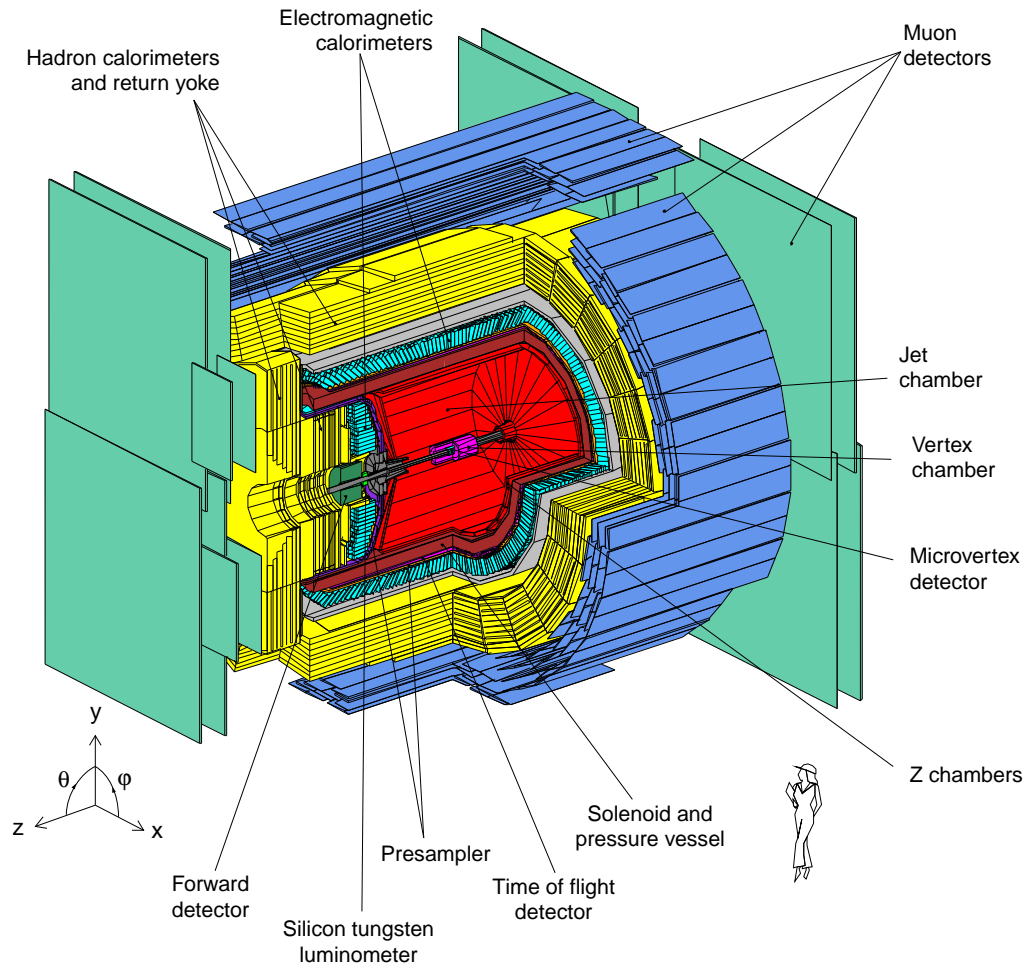


Figure 3.2: An outline overview of the OPAL detector.

Its general layout is shown in figure 3.2. The detector is made up of many subsystems, but can be divided into three main parts: (1) the central detector surrounded by (2) the calorimeters and (3) the muon system. Due to the cylindrical geometry, most subsystems are divided in a barrel part and the endcaps. The detector has a length of 12 m and a diameter of 10 m.

A right-hand cartesian coordinate system is used to describe data taken at OPAL. The x-axis points to the center of the LEP ring, the z-axis is defined by the direction of the

electron beam and the y-axis points perpendicular upwards from the x-z plane. Instead of cartesian coordinates, tracks measured in the detector are often parametrized in polar coordinates, the polar angle θ is counted from the z-axis, the azimuthal angle ϕ from the x-axis.

An overview of the main elements is given here, starting from the inner parts and progressing to the outer parts of the detector.

3.2.1 The Central Detector

The Central Detector is inside a solenoid supplying a uniform magnetic field of 0.435 T oriented along the z-axis. The central detector consists of a Microvertex detector, a precision vertex detector, a large volume jet chamber and surrounding Z-chambers situated inside a pressure vessel holding a pressure of 4 bar.

Around the beam pipe in the vicinity of the collision point the Silicon Microvertex detector is placed. It consists of silicon microstrip counters. This detector is mainly used to measure secondary vertices, e.g. of B-meson decays. Typical resolution for the point of closest approach of the highest energy track to the interaction point is $15 \mu\text{m}$ in the $r - \phi$ plane and $20 - 50 \mu\text{m}$ in the z direction.

The vertex detector is a high precision cylindrical jet drift chamber located between the beam pipe and the jet chamber. It is 100 cm long and has a diameter of 47 cm. The chamber consists of an inner layer of 36 cells with axial wires and an outer layer of 36 small angle stereo cells (4° with respect to the beam axis). The vertex detector allows to locate decay vertices of short lived particles in the $r - \phi$ plane and the determination of the z coordinate.

The main tracking of the particles is performed with the jet chamber. It is a cylindrical drift chamber of 400 cm in length and 370 cm in diameter. The chamber consists of 24 identical sectors each containing a wire plane of 159 wires aligned parallel to the beam direction providing both high redundancy and high precision for the reconstruction of multihadronic events.

The jet chamber is filled with an argon/methan/isobutane gas mixture at 4 bar pressure. The reconstruction of tracks in drift chambers is based on the ionization of the chamber gas by the transversing particles and on a measurement of the drift time of the liberated electrons to the signal wires which are kept on a positive high voltage [21, 22]. Particle momenta can be determined from the curvature of the reconstructed tracks in the magnetic field.

The jet chamber allows a particle identification via the measurement of the specific energy loss dE/dx by summing the charge received at both ends of a wire.

The central detector is completed by the surrounding Z-chambers which provide a precise measurement of the z coordinate (and therefore the polar angle θ) of tracks as they leave the jet chamber.

The central detector achieves a momentum resolution of

$$\frac{\sigma_{p_t}}{p_t} = \sqrt{(0.02)^2 + (0.0015 p_t)^2}, \quad (3.4)$$

where p_t is the transverse momentum of the particles, i.e. the momentum in the x-y plane. Its average angular resolution is about 0.3 mrad in ϕ and 1 mrad in θ .

3.2.2 The Time-of-Flight Detector (TOF),

The Time-of-Flight Detector surrounding the central detector and the magnet coil, is made of 160 scintillators (650 cm in length, 9 cm in width). Charged particles excite the scintillator material and lead to emission of photons which are measured by photomultipliers at both ends of the TOF bars. In conjunction with a beam crossing signal, the TOF allows to measure the flight time of charged particles from the interaction point to the subdetector. The Time-of-Flight detector is a major part of the OPAL trigger system. By measuring the time of flight and the pulse height of the produced signals, particles in the momentum range of 0.6 – 2.5 GeV can be identified. An effective rejection of cosmic rays is also performed.

3.2.3 The Calorimeter System

The calorimeter system surrounding the central detector and the time-of-flight detector is used to measure the energy of charged and neutral particles. Unlike the tracking chambers, which are low density position measuring devices used to determine the momentum and the direction of the particle, the calorimeters are designed as total absorption detectors for the purpose of stopping all impinging particles.

The interaction mechanism of particles with matter depends on whether they interact by the strong force or not. Therefore the calorimeter system consists of two subdetectors: the electromagnetic calorimeter and the hadron calorimeter.

The electromagnetic calorimeter (ECAL) encloses the magnet. It identifies and measures the energies of electrons, positrons and photons. The ECAL consists of 11704 lead glass blocks split into a barrel part and two endcap arrays. The segmentation of the calorimeter allows also the measurement of the track angles and the matching of clusters with the tracking information taken from the inner drift chambers. For this purpose the lead blocks are pointing towards the interaction region in the barrel part and are parallel to the z-axis in the endcaps. This arrangement together with two forward lead scintillator calorimeters of the forward detectors makes the OPAL acceptance for electron and photon detection almost equal to 99% the solid angle 4π . Čerenkov light from the passage of relativistic charged particles through the lead glass is detected by 3 inch diameter phototubes at the base of each block.

The intrinsic resolution of the ECAL in the barrel region is

$$\frac{\sigma_E}{E} = 0.26\% + \frac{6.3\%}{\sqrt{E}} \quad (3.5)$$

and for the endcaps

$$\frac{\sigma_E}{E} = \frac{5\%}{\sqrt{E}} \quad (3.6)$$

The extension of at least 22 radiation lengths of the ECAL ensures that the electromagnetic showers are always contained within the calorimeter. The presence of approximately two radiation lengths of material in front of the calorimeter (mostly due to the solenoid and pressure vessel), results in most electromagnetic showers that are initiated before reaching the lead glass of the ECAL.

Presampling devices are therefore installed between the TOF and the ECAL to measure the position and charge multiplicity of electromagnetic showers as they enter the

electromagnetic calorimeter. These measurements are used to derive energy corrections in order to improve energy resolution of the ECAL itself and give additional γ/π^0 and electron/hadron discrimination.

The hadron calorimeter (HCAL) surrounds the electromagnetic calorimeter. It is build as a sampling calorimeter with alternate layers of active and passive material, and is used for the energy measurement of hadrons. The passive layers are formed by the iron return yoke of the solenoid magnet and the active layers consist of streamer chambers, offering at least four interaction lengths of iron absorber to particles emerging from the electromagnetic calorimeter. Essentially all hadrons are absorbed at this stage leaving only muons to pass on into the surrounding muon chambers. In order to measure the hadronic energy correctly, the hadron calorimeter information must be used in combination with that from the preceding electromagnetic calorimeter.

Compared to the electromagnetic calorimeter, the resolution is worse due to larger fluctuations present in hadronic showers and reaches only

$$\frac{\sigma_E}{E} \approx \frac{120\%}{\sqrt{E}}. \quad (3.7)$$

3.2.4 The Muon System

The outermost subdetector of OPAL is the muon system. It aims to identify muons in an unambiguous way from a potential hadron background. Besides the undetected neutrinos, muons are the only particles not stopped in the calorimeters. The muon system consists of four planar drift chamber layers in the barrel region and limited-streamer tubes in the endcaps. The direction of a muon track can be determined from the hit coordinates in the individual layers. Muons created in the initial processes of the e^+e^- collisions can be distinguished from secondary muons (produced in the secondary showers in the calorimeters) and cosmic muons by comparing the hits in the muon chambers with the information provided by the central tracking system.

3.2.5 The Forward Detector and the SiW Luminometer

At OPAL the measurement of Bhabha events is performed by the forward detector which is a set sampling of calorimeters and drift tubes and the silicon tungsten luminometer which is a sampling calorimeter. By measuring the event rate of low Bhabha scattering $e^+e^- \rightarrow e^+e^-$ events the luminosity delivered by the LEP accelerator to the OPAL experiment can be determined.

3.2.6 The Trigger and Data Acquisition

With four electron and four positron bunches at LEP, the bunch crossing rate for OPAL detector is $22 \mu\text{s}$. Events are only recorded by the data acquisition system if they satisfy certain trigger conditions. This selection is done on-line reducing the number of events to about 10 in a second. Once the trigger logic selects a potentially interesting event, the subdetectors are read out separately. The information of all subdetectors is then combined by the event-builder and sent to the filter. From the filter the data are written to files and reconstructed as soon as the required calibration constants are available. Data are often available for analysis within a few hours after the end of a run.

Chapter 4

Data and Monte Carlo Samples

4.1 Data Samples

The present analysis is based on data collected by the OPAL detector in the years 1998 and 2000 at center-of-mass energies in the range from 189 GeV to 206 GeV. The data collected in the year 1999 is not investigated in the present analysis, due to the small values of the integrated luminosities at a center-of-mass energy of $\sqrt{s} = 192, 196$ GeV. The center-of-mass energies at which data were recorded are depicted in Figure 4.1.

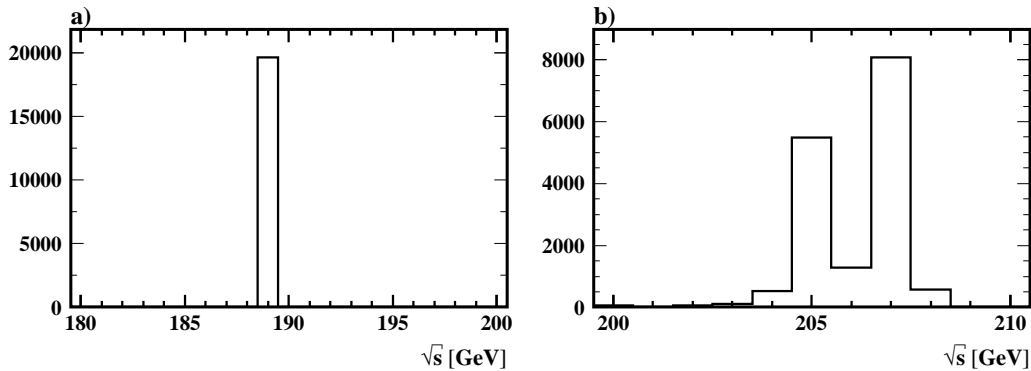


Figure 4.1: The center-of-mass energy for collected data in (a) 1998 and (b) 2000.

The center-of-mass energy $\sqrt{s} = 206$ GeV is a mean value of collected data, while the integrated luminosities at 205, 207 GeV have the highest values.

The present analysis uses a subset of data samples for which the necessary detector components were operating during the recording. Therefore the data represent an integrated luminosity \mathcal{L} of

$$\mathcal{L} = 172 \text{ pb}^{-1} \text{ for } \sqrt{s} = 189 \text{ GeV} \quad (4.1)$$

$$\mathcal{L} = 211 \text{ pb}^{-1} \text{ for } \sqrt{s} = 206 \text{ GeV} \quad (4.2)$$

collected by the OPAL detector. In addition, 11.3 pb^{-1} of calibration data were collected at $\sqrt{s} = m_Z$ in the years 1998-2000 and have been used for fine tuning of the Monte Carlo simulation.

4.2 Monte Carlo Samples

The OPAL detector response is simulated using the GEANT [23] algorithm, which takes into account the energy loss, multiple scattering and showering in the detector. The hadronisation process is simulated using JETSET with parameters described in reference [24] and the W boson mass set to $m_W = 80.33$ GeV.

4.2.1 Signal

Samples of fully simulated events were produced for the final state at different center-of-mass energies. Considering the uncertainty in the top mass ($m_t = 174.3 \pm 5.1$ GeV [5]) the signal Monte Carlo samples were generated for three different values of the top mass (169, 174 and 179 GeV).

The process of $Z/\gamma \rightarrow t\bar{q}$ was simulated with the generator PYTHIA [25]. According to this simulation the top quark is produced together with a light quark via an s-channel exchange of a boson and forced to decay into bW before building a bound state. The beauty and the charm quark are joined by a string to form a color singlet. All couplings and QCD effects are the same as in Z decays to light quarks. Initial state radiation from soft and hard photon bremsstrahlung contributions are included. The top quark is assumed to have a 100% branching ratio to Wb . This is not strictly true if the couplings are equal to their CDF limits, where $BR(t \rightarrow Zc)$ could be as high as 33+3% (Eq:(2.8)).

4.2.2 Background

Single top quark events are characterized by the presence of a W boson decaying into a lepton and a neutrino, a beauty quark jet and a light quark jet. Therefore the principal background will be due to $WW+ZZ$ and QCD events.

The backgrounds simulated for the investigated signal events are:

- QCD: $(Z/\gamma)^* \rightarrow q\bar{q}(\gamma)$, called qq
- $WW+ZZ$: $e^+e^- \rightarrow W^+W^-$, $e^+e^- \rightarrow ZZ$, called 4f
- two-photon: $e^+e^- \rightarrow \gamma\gamma$, called $\gamma\gamma$

For background studies, the qq and 4f event samples corresponding to integrated luminosities at much higher values than the data were generated. Therefore the statistical error produced by the Monte Carlo samples is small.

The qq background was simulated using PYTHIA. Grc4f [26] was used to simulate the four-fermion processes 4f. The $\gamma\gamma$ background was simulated using PYTHIA and PHOJET [27] and has much lower luminosity than the collected data. This background is negligible after the first cuts are applied .

In order to simulate the background processes close to the collected data, all Monte Carlo samples used in the next chapter are scaled to the corresponding integrated luminosity of the data taken by the OPAL detector. Since the background simulations include Standard Model processes only, any excess observed in the data, would signal the existence of new physics.

Chapter 5

Single Top Quark Analysis

The search of single top quark production in the semi-leptonic decay channel is investigated, using two data samples collected by the OPAL detector with an integrated luminosity of $\mathcal{L} = 172 \text{ pb}^{-1}$ at $\sqrt{s} = 189 \text{ GeV}$ and $\mathcal{L} = 211 \text{ pb}^{-1}$ at $\sqrt{s} = 206 \text{ GeV}$. The analysis is carried out at the former center-of-mass energy. By applying the same cuts and using the same variables for the likelihood function, the latter is then investigated.

The leptonic decays of the W boson are taken into account. Therefore only the simulated leptonic decays in the signal Monte Carlo $\text{BR}(W \rightarrow l\nu) \sim 33\%$ are used.

First, a global event selection and preselection cuts are applied based on Monte Carlo samples only. These cuts efficiently reduce the background while retaining the signal. This is especially effective against background from low multiplicity events, two-photon interactions and events with no missing energy in the final state.

Second, a final set of variables is chosen to construct a discriminating variable using a standard likelihood selection method. The results for possible single top quark production are deduced.

5.1 Event Selection

5.1.1 Global Event Selection

Several standard event selections are made during processing data of the OPAL detector. Events are reconstructed from the detection of tracks in the central detector and of clusters in both calorimeters (electromagnetic and hadronic). Because of the presence of two jets in a single top quark event in the semi-leptonic decay channel, high multiplicity hadronic events are selected with at least 7 calorimeter clusters, 5 tracks and the total visible energy larger than 14% of the total center-of-mass energy [28]. These cuts remove all events with low multiplicity, low energy in the final state and therefore reject a large portion of $\gamma\gamma$ events.

To prevent energy double-counting of the tracks and their associated clusters, the total visible energy E_{vis} and momenta \vec{p}_{vis} , of the event and of the individual jets are corrected using a matching algorithm [29, 30].

5.1.2 Lepton Identification

The presence of an isolated lepton is required for the leptonic channel. The lepton identification is performed by using a neural network [31], designed to address the issues at LEP2. The algorithm is track-based, i.e. real tau decay tracks are efficiently separated from those tracks arising from the hadronic system. The neural net (NN) is efficient for detecting all lepton flavors (e, μ, τ).

The tracks in the event are considered one by one in decreasing order of momentum as 'seed' tracks. Before describing the input variables of the NN it is useful to define two cones, both having the momentum vector of the seed track as their common axis. The 'narrow' cone has a 10° half-angle; the 'annular' cone has a 30° half-angle and excludes the narrow cone. The input variables are related to the invariant mass of all tracks and clusters (corrected with the matching algorithm [29]) in the narrow cone, the total energy of all particles in the narrow cone, the ratio of the total energy in the annular cone to the total energy in the narrow cone, the number of particles with energy greater than 750 MeV in the annular cone and the total energy of all charged tracks in the annular cone. The variables were chosen in order to maximize both the neural net's final discrimination power and the data/Monte Carlo agreement of the input.

Lepton candidates subject to the present analysis are classified as one-prong candidates within the NN: each lepton candidate has a momentum larger than 2 GeV and no other tracks in a conus of 10° must be detected. Tracks consistent with having originated from a photon conversion are excluded within the NN.

5.1.3 Jet finding

After removing the lepton, exactly two jets are reconstructed from the remaining clusters with the DURHAM algorithm [32, 33]. According to this algorithm, for each pair of final-state particles (i, j) the scaled transverse momentum y_{ij} is given by

$$y_{ij} = 2 \frac{\min(E_i^2, E_j^2)(1 - \cos\theta_{ij})}{E_{\text{vis}}^2} \quad (5.1)$$

where E_{vis} is the energy of the remaining hadronic part, E_i and E_j are the energies of the particles i and j at relative angle θ_{ij} . Once the smallest value of y_{ij} is found, the corresponding particles (i, j) form a 'pseudo-particle' (by adding their four-momentum vectors). This process is iterated until the number of pseudo-particles equals the required jet number, which is 2 in the present case. These remaining pseudo-particles are called jets. The minimum of y_{ij} for these two final jets is called the jet resolution parameter y_{12} at which the number of jets passes from two to one.

5.1.4 b-Tagging

Signal events are known to have a low energetic charm jet and a high energetic beauty jet. The tagging of jets originating from a beauty quark is an important tool in single top production searches. A b-tagging package is therefore applied [34, 35]. This jet-wise b-tagging algorithm, which has been developed for the Higgs boson search, uses three independent b-tagging methods, namely (1) lifetime information, (2) lepton

high- p_t (transverse momentum) and (3) jet kinematics. A global combination of these three methods is performed with an unbinned likelihood technique to form a single discriminating variable for each jet.

5.2 Motivation for Preselection Cuts and Likelihood

The signal cross section σ_{stop} is not expected to be very large for values of the anomalous couplings which are consistent with model expectations. Yet the final state is quite characteristic in comparison with the background events (Fig. 5.1).

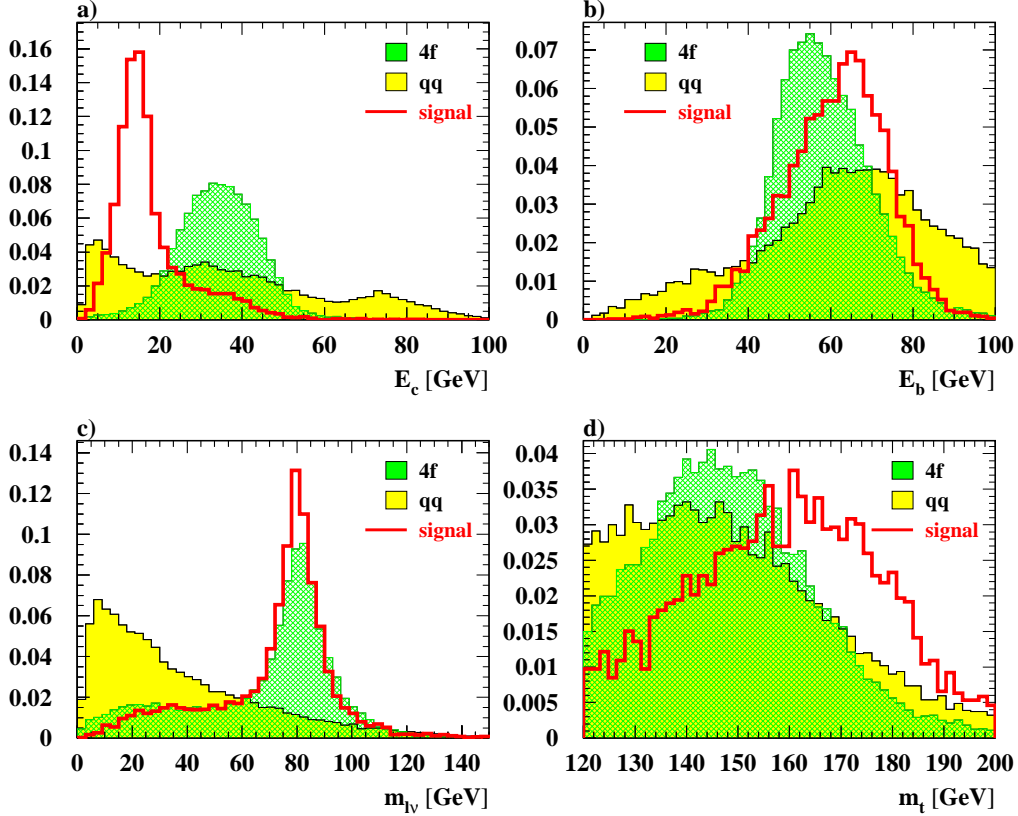


Figure 5.1: Normalized distribution for the final state topology characteristics at $\sqrt{s} = 189$ GeV. Only events with an isolated lepton in the final state are selected. The 4f background is indicated in green (hatched grey), the background arising from qq decay in yellow (light grey) and the signal as a red (solid) line. Plot (a), (b) show jet energy distributions E_c , E_b , (c) the reconstructed mass $m_{l\nu}$ and (d) the reconstructed top quark mass m_t .

The distributions are normalized to unity and shown on detector level. The background from WW decays is indicated in hatched green, the background arising from qq decays in yellow and the signal as a red line. Only events satisfying the lepton identification cut (described in section 5.1.2) are selected. The Standard Model background (WW,

ZZ, qq) is therefore reduced. In the present analysis no attempt is made to identify the light quark flavor.

- Due to two-body kinematics of the signal, the charm jet has nearly fixed energy values of $E_c \sim 15$ GeV at $\sqrt{s} = 189$ GeV (Fig. 5.1 (a)). In contrast to the energy of the signal charm jet, which has a small distribution around the expected energy, the corresponding background is uniformly distributed.
- Similarly, the energy of the selected jet with the higher energy in the signal (as a jet originating from the beauty quark decay) is typically $E_b \sim 65$ GeV at $\sqrt{s} = 189$ GeV (\pm smearing from the top quark motion) (Fig. 5.1 (b)).

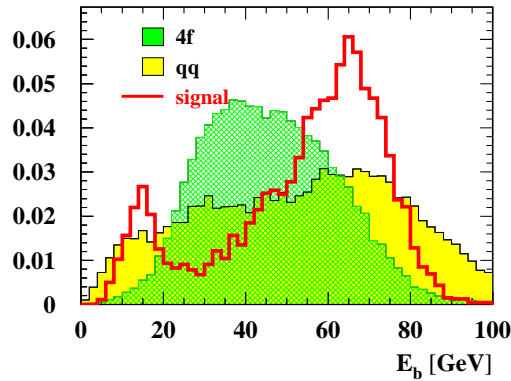


Figure 5.2: The energy of the jet with the higher b-tag probability. About $\sim 15\%$ of the events are misidentified. Colors apply as in Figure 5.1.

Only the kinematic signature is used to select the jet originating from a beauty quark. By selecting the jet with the higher b-tag probability low energetic jets arising from the charm quark decay would be identified as beauty jets. A misidentification in about $\sim 15\%$ of the events can be avoided by selecting the beauty jet with the applied method. Additionally the b-tag probability for the selected jet can now be used to efficiently separate the semi-leptonic WW background from the signal.

- The distribution of the reconstructed invariant mass $m_{l\nu}$ of the signal has the peak as expected at $m_{l\nu} \sim 80$ GeV, due to the W boson mass. The corresponding background is apparently different. Only the distribution of products from W pair production peaks at similar values (as one W boson decays leptonically and one hadronically).
- The mass distribution of the reconstructed top quark m_t is shown in Figure 5.1 (d). As the top quark is assumed to decay into a W boson and a beauty jet, its mass can be reconstructed from their decay products. The distribution of the reconstructed mass for the signal peaks at $m_t \sim 168$ GeV, while the background distributions show lower reconstructed masses.

At higher energies the signal distribution is kinematically not well separated from the background distribution: signal and 4f background distribution (mainly semi-leptonic WW events) overlap.

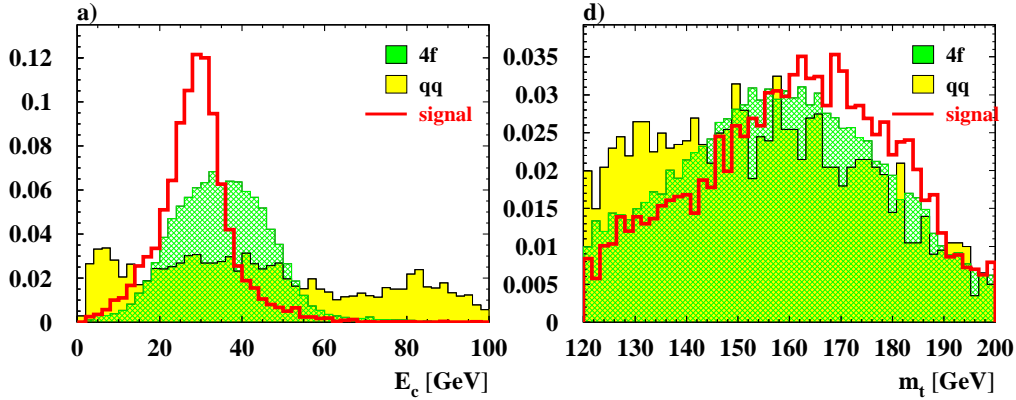


Figure 5.3: Normalized distributions for the final state topology characteristics at $\sqrt{s} = 206$ GeV. Only events with an isolated lepton in the final state are selected. (a) shows the jet energy distribution E_c , (b) the reconstructed top quark mass m_t . Colors apply as in Figure 5.1.

The energy distribution of the jet arising from the charm quark E_c and the reconstructed top quark mass m_t at $\sqrt{s} = 206$ GeV is shown in Figure 5.3. Both distributions evidence higher overlapping than for $\sqrt{s} = 189$ GeV .

Due to this fact, the distribution of the final discriminating variable will have a different shape for $\sqrt{s} = 206$ GeV than for $\sqrt{s} = 189$ GeV.

5.3 Preselection for Single Top Candidates

In order to reduce the SM background that has a totally different topology than the signal Monte Carlo, preselection cuts are applied. The preselection aims to reject all SM processes which do not have two jets, one isolated lepton and missing transverse momentum in the final state. The same cuts are applied for $\sqrt{s} = 189$ GeV and $\sqrt{s} = 206$ GeV center-of-mass energies.

In all following figures the signal is normalized to the luminosity assuming to have a cross section of $\sigma_{\text{stop}} = 3$ pb and indicated as a red (solid) line. The Monte Carlo Simulation is indicated in green (dark grey) for the 4f background, in yellow (light grey) for the qq background and in blue (black) for the $\gamma\gamma$ background. All backgrounds are added up and subsequently are compared to the data.

The preselection cuts are applied successively in order of their appearance starting with the lepton identification.

Preselection cuts

- (1) **NN-output**,
only events with an isolated lepton in the final state are investigated. Therefore only candidates detected by the NN are selected as lepton candidates. If there is more than one isolated lepton in an event, the lepton with the highest NN output is taken as the candidate lepton. No attempt is made to distinguish between different lepton flavors. All decays to e, μ, τ leptons are considered. For the τ lepton the modes with one charged particle (1-prong) are considered only.
- (2) **$|\cos\theta_{\text{miss}}| < 0.9$** ,
where $\cos\theta_{\text{miss}}$ is the cosine of the polar angle of the missing momentum vector calculated from the visible momentum vector as: $\vec{p}_{\text{miss}} = -\vec{p}_{\text{vis}}$ (energy-momentum conservation in the center-of-mass-frame).
This distribution is shown in Figure 5.4 and 5.7 for both center-of-mass energies. The cut is indicated as black vertical lines at $|\cos\theta_{\text{miss}}| = 0.9$. An apparent difference between the signal and QCD background qq as well as 4f background can be observed. As the signal is uniformly distributed, the background distribution qq shows peaks for events with missing momentum along the beam pipe due to initial state radiation along the beam pipe. This cut rejects very effectively the radiative Z returns (QCD).
- (3) **$50 \text{ GeV} < \Sigma p_t^{\text{vis}} < 170 \text{ GeV}$** ,
where Σp_t^{vis} is the scalar sum of the transverse visible momentum of the event. The requirement $50 \text{ GeV} < \Sigma p_t^{\text{vis}}$ avoids the visible momentum to be along the beam direction, while $\Sigma p_t^{\text{vis}} > 170 \text{ GeV}$ rejects events with no missing energy in the final state.
The distributions are shown in Figure 5.5 and 5.8 for both center-of-mass energies. The cuts are indicated as black vertical lines at $\Sigma p_t^{\text{vis}} = 50 \text{ GeV} (170 \text{ GeV})$. These cuts remove what is left of the $\gamma\gamma$ background. This background shows too few entries at $\sqrt{s} = 206 \text{ GeV}$ due to its small integrated luminosity (Fig. 5.8). After all preselection cuts, the $\gamma\gamma$ background is completely negligible (see Table 5.1). In addition signal events have higher missing energy in the final state than those arising from the background.
- (4) **$p_t^{\text{miss}} > 25 \text{ GeV}$** ,
where p_t^{miss} is the transverse missing momentum of the event.
The distribution is shown in Figure 5.6 and 5.9 for both center-of-mass energies. The cut is indicated as a black vertical line at $p_t^{\text{miss}} = 25 \text{ GeV}$.
This cut rejects events with low missing energy in the final state, as only events with high missing energy must be selected. Only the semi-leptonic WW background shows higher values but lower as the signal ones.

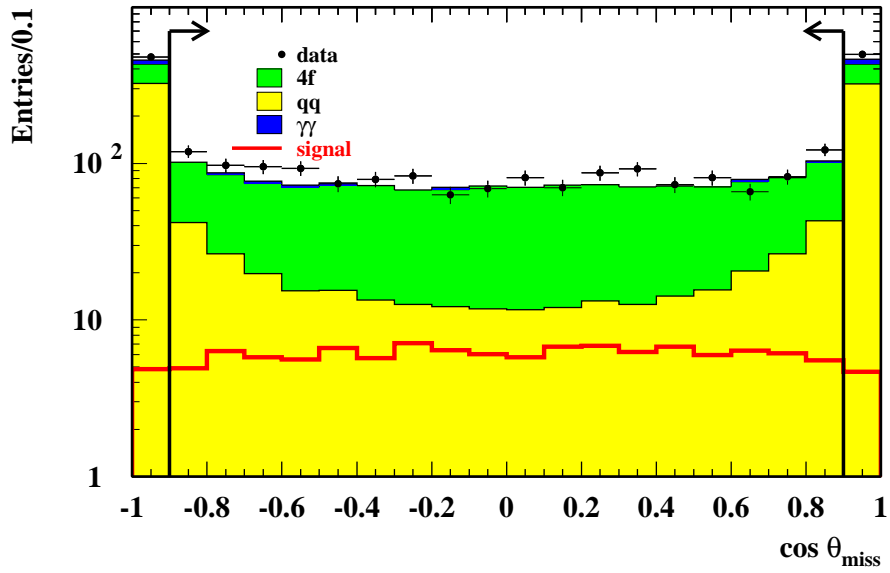


Figure 5.4: The distribution of $|\cos\theta_{\text{miss}}|$ for $\sqrt{s} = 189$ GeV. All previous cuts are applied.

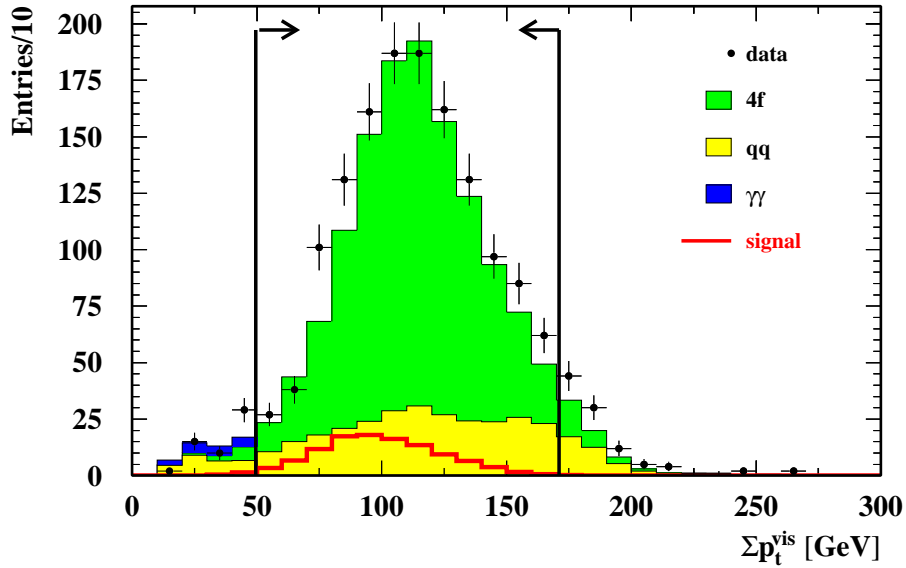


Figure 5.5: The distribution of Σp_t^{vis} for $\sqrt{s} = 189$ GeV. All previous cuts are applied.

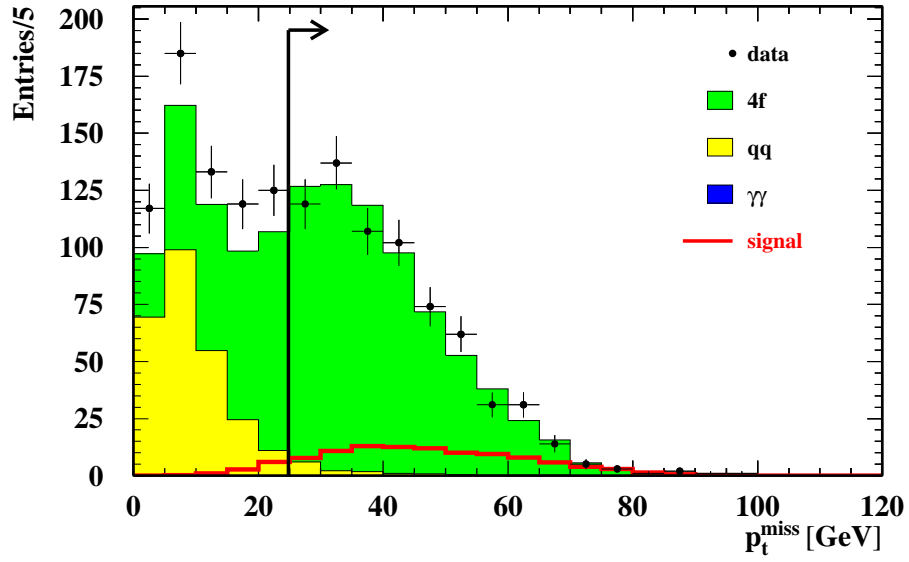


Figure 5.6: The transverse missing momentum for $\sqrt{s} = 189$ GeV. All previous cuts are applied.

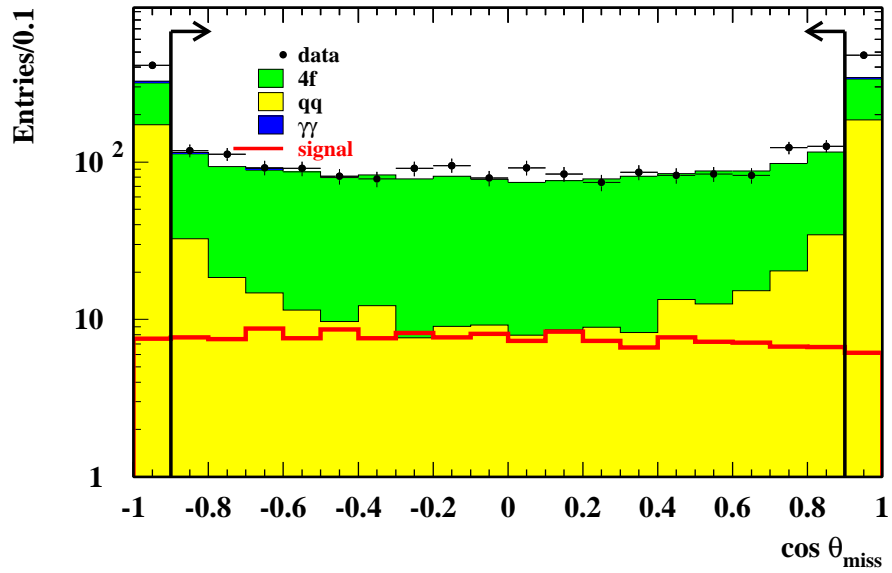


Figure 5.7: The distribution of $|\cos\theta_{\text{miss}}|$ for $\sqrt{s} = 206$ GeV. All previous cuts are applied.

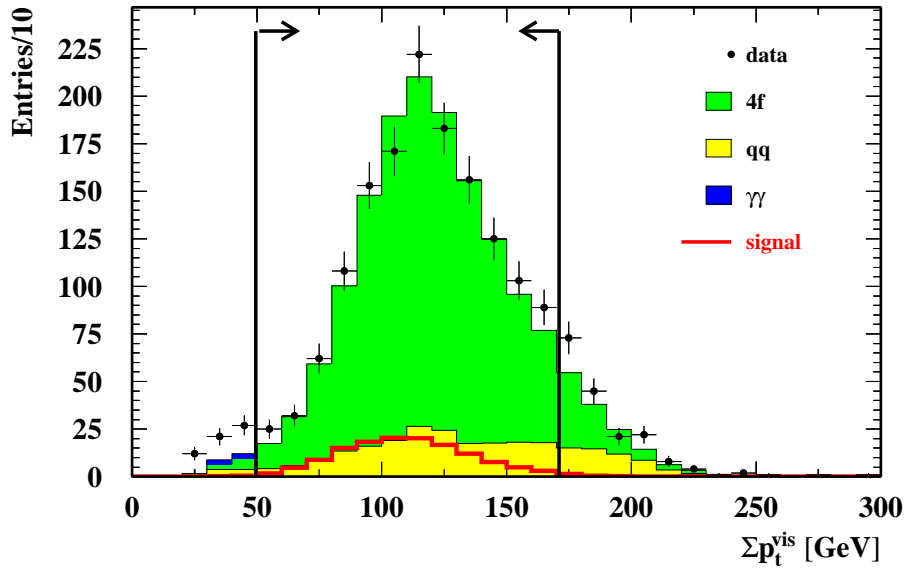


Figure 5.8: The distribution of Σp_t^{vis} for $\sqrt{s} = 206$ GeV. All previous cuts are applied.

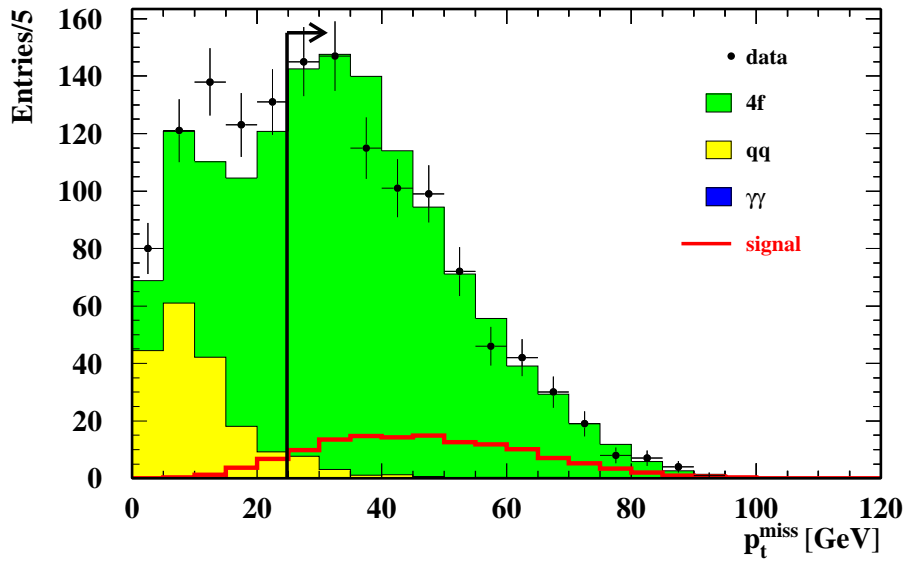


Figure 5.9: The transverse missing momentum for $\sqrt{s} = 206$ GeV. All previous cuts are applied.

Cut-flow-tables The choice of kinematical cuts is very efficient in reducing the size of the background (Bdg), while retaining the signal. A cut-flow-table for both center-of-mass energies (189 GeV, 206 GeV) is delineated in Table 5.1 and 5.2.

cut	Data	Total Bgd	llqq	q \bar{q}	4f	$\gamma\gamma$	$\epsilon \cdot \text{BR} \%$
no cut	18177	17553.7	1404.7	13923.6	1799.7	425.7	29.6
NN-output	2498	2234.3	976.1	982.5	275.7	73.2	23.1
$ \cos\theta_{\text{miss}} $	1526	1372.1	886.5	337.7	147.9	15.5	21.3
Σp_t^{vis}	1369	1266.6	871.7	271.8	123.2	0.0	20.8
p_t^{miss}	690	683.0	666.9	12.8	3.3	0.0	18.9

Table 5.1: Cut-flow table for data and Monte Carlo samples at $\sqrt{s} = 189$ GeV and $\mathcal{L} = 172 \text{ pb}^{-1}$.

cut	Data	Total Bgd	llqq	q \bar{q}	4f	$\gamma\gamma$	$\epsilon \cdot \text{BR} \%$
no cut	16210	15380.5	1835.5	11049.6	2255.2	240.2	30.3
NN-output	2557	2223.6	1269.7	615.8	338.2	28.3	23.5
$ \cos\theta_{\text{miss}} $	1670	1566.1	1137.1	256.6	172.4	4.7	21.4
Σp_t^{vis}	1429	1400.7	1091.6	189.7	119.3	0.0	20.9
p_t^{miss}	836	874.2	856.4	13.3	4.5	0.0	19.0

Table 5.2: Cut-flow table for data and Monte Carlo samples at $\sqrt{s} = 206$ GeV and $\mathcal{L} = 211 \text{ pb}^{-1}$.

The data shows a good agreement with the Monte Carlo expectations for the background. The signal efficiency multiplied by the leptonic decay branching ratio of the W boson is reduced to $\sim 19.0\%$ for both center-of-mass energies (Table 5.1, 5.2). It is independent of the flavor of the light quark (c/u) produced with the top and of whether the W decays to an electron, muon or tau.

The $\gamma\gamma$ background is negligible after removing events with low missing energy in the final state. The qq background arising from QCD events is efficiently reduced. According to the MC simulation, the background passing this preselection is composed of: q \bar{q} events, semi-leptonic WW events (llqq) and other 4 fermion events (qqqq).

Fortunately the irreducible background arising from $e^+e^- \rightarrow W^+W^- \rightarrow \bar{c}b l \nu$ events is negligible due to the small size of the CKM mixing matrix element $U_{cb} = 0.0402 \pm 0.0019$ [5].

Nevertheless the leading background comes from $e^+e^- \rightarrow W^+W^- \rightarrow qq'l\nu$, where qq' are light quarks (labeled as llqq in Table 5.1, 5.2). The tagging of beauty jets is therefore an efficient requirement for rejecting the llqq background.

5.4 Likelihood Selection

A final discriminating variable is constructed in order to efficiently select the signal type events and reject the background type ones. This is adequate as the sample size is small and the distributions consists of essentially uncorrelated variables.

The final discriminating variable is achieved by using a vector of measurements \mathbf{x} , on the basis of a single quality \mathbf{L} [36, 37],

$$\mathbf{L} = \frac{P_{\text{signal}}(\mathbf{x})}{P_{\text{signal}}(\mathbf{x}) + P_{\text{background}}(\mathbf{x})}, \quad (5.2)$$

where P_{signal} and $P_{\text{background}}$ are the probability density functions for two categories of events. The optimal event-classification scheme selects events having the largest values for the ratio of probabilities $P_{\text{signal}}(\mathbf{x})/P_{\text{background}}(\mathbf{x})$ to define a sample enriched in signal events.

Each event is classified on the basis of whether or not the value of \mathbf{L} for that event is larger than some critical value. Signal events tend to have a value of \mathbf{L} near 1, whereas background events near 0.

The probability density functions P_{signal} and $P_{\text{background}}$ are determined from the product of Monte Carlo 1-dimensional distributions (or reference distributions) of the input variables:

$$P_{\text{signal/background}}(\mathbf{x}) = \prod_i P_i. \quad (5.3)$$

If three classes of events (signal, two backgrounds) are classified, the P_i require to be renormalized to their abundances.

For each event satisfying the preselection cuts a binned likelihood function is constructed, with one class for the signal, one for the qq background and one for the semi-leptonic WW (llqq) background. The following variables are used to construct this final discriminating variable.

Likelihood Variables

- (1) The invariant mass \mathbf{m}_{ν} from the W decay.

The invariant mass for the decaying particle X is calculated as:

$$m_X^{\text{inv}} = \sqrt{\left(\sum_i p_i\right)^2} = \sqrt{\left(\sum_i E_i\right)^2 - \left(\sum_i \vec{p}_i\right)^2} \quad (5.4)$$

where p_i is the four-momentum vector, E_i the energy and \vec{p}_i the three-momentum vector of the lepton and the neutrino, respectively. The missing four-momentum vector is obtained as follows:

- from the missing three-momentum vector

$$\vec{p}_{\text{miss}} = -\vec{p}_{\text{vis}} \quad \Rightarrow \quad p_{\text{miss}} = (p_{\nu,x}, p_{\nu,y}, p_{\nu,z}) \quad (5.5)$$

– and assuming the missing mass to be zero

$$m_{\text{miss}} = 0 \quad \Rightarrow \quad E_{\text{miss}} = \sqrt{p_{\nu,x}^2 + p_{\nu,y}^2 + p_{\nu,z}^2} \quad (5.6)$$

The distribution of the variable $m_{l\nu}$ is shown in Figure 5.10 (a) ($\sqrt{s} = 189$ GeV) and Figure 5.11 (a) ($\sqrt{s} = 206$ GeV). Signal events and semi-leptonic WW events have a peak at $m_{l\nu} \sim m_W$ as the lepton and neutrino are products of one W decay. Lower masses are reconstructed for the qq background as no events from W decay are expected. In certain events a lower mass $m_{l\nu}$ at ~ 30 GeV is reconstructed due to τ lepton events.

- (2) The invariant mass m_{qq} of the remaining hadronic part (2 jets).
The invariant mass is calculated using equation (5.4), where p_i is the four-momentum vector, E_i the energy and \vec{p}_i the three-momentum vector of the hadronic part. The energies and momenta of the jets are well known.
The distribution of the variable m_{qq} is shown in Figure 5.10(b) and 5.11(b) for both center-of-mass energies. The di-jet invariant mass for the llqq background events primarily reconstructs to the W boson mass. It assumes lower values for the signal where it provides the mass of the beauty and charm jet.
- (3) The logarithm of the DURHAM jet resolution parameter $\ln(\mathbf{y}_{12})$.
The variable y_{12} is calculated as described in section 5.1.3.
The distribution of $\ln(y_{12})$ is shown in Figure 5.10(c) and 5.11(c) for both center-of-mass energies. According to y_{12} the signal jets are separated more efficiently as the background jets due to the boost of the W system at higher energies.
- (4) The momentum \mathbf{p}_{qq} of the remaining hadronic part.
This variable is also shown in Figure 5.10(d) and 5.11(d) for both center-of-mass energies. The variable implies higher momenta for the signal jets and lower values for those arising from the background, as the background quarks are known to be light quarks and therefore having lower momenta.
- (5) The b-tag probability P_b for the selected beauty jet.
The jet with the higher energy is selected as the beauty jet. The signal probability P_b for the selected jet is apparently different compared to the background. It has a probability of P_b near 1 to be correctly identified, while the probability for the background jet has small values of P_b near 0.
The quarks arising from the semi-leptonic WW events are light quarks. Therefore the b-tag probability P_b is an efficient variable, because it clearly distinguishes between the signal and the WW (llqq) background for both center-of-mass energies. In certain events P_b is ~ 0.15 , due to misidentified charm jets (section 5.2). The distributions are shown in Figure 5.10(e) and 5.11(e) for both center-of-mass energies.

The dominating SM background comes from the semi-leptonic WW background llqq for both center-of-mass energies. At $\sqrt{s} = 206$ GeV the distributions of the selected variables for the signal and the WW background overlap. This fact decreases the discrimination power between signal and background. Only the b-tag variable P_b shows an apparently different distribution for the signal as for the background.

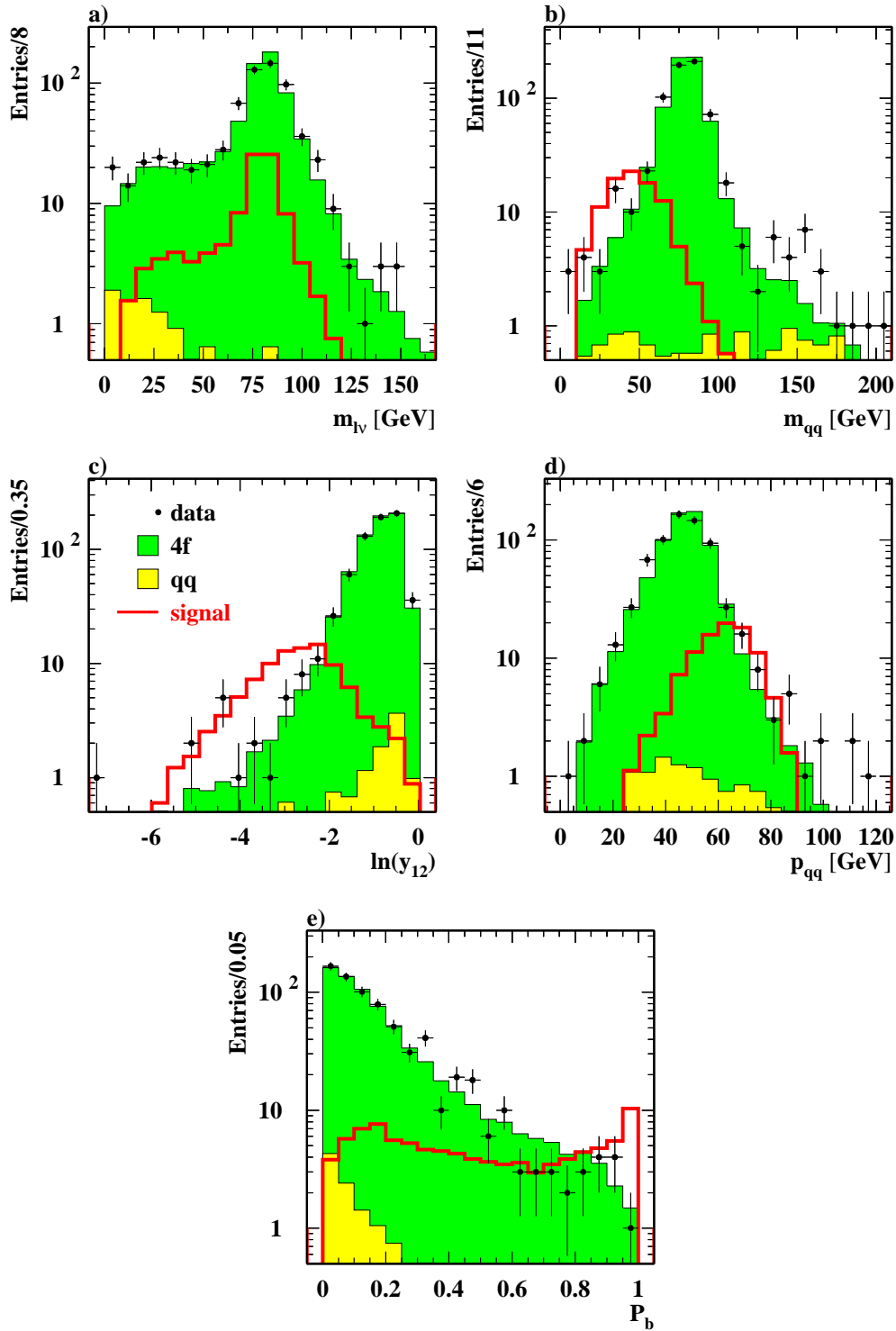


Figure 5.10: Likelihood variables at $\sqrt{s} = 189$ GeV: (a) reconstructed invariant mass of the W boson $m_{l\nu}$, (b) mass of the di-jet system m_{qq} , (c) jet resolution parameter $\ln y_{12}$, (d) momentum of the di-jet system p_{qq} and (e) b-tag probability P_b for the selected beauty jet.

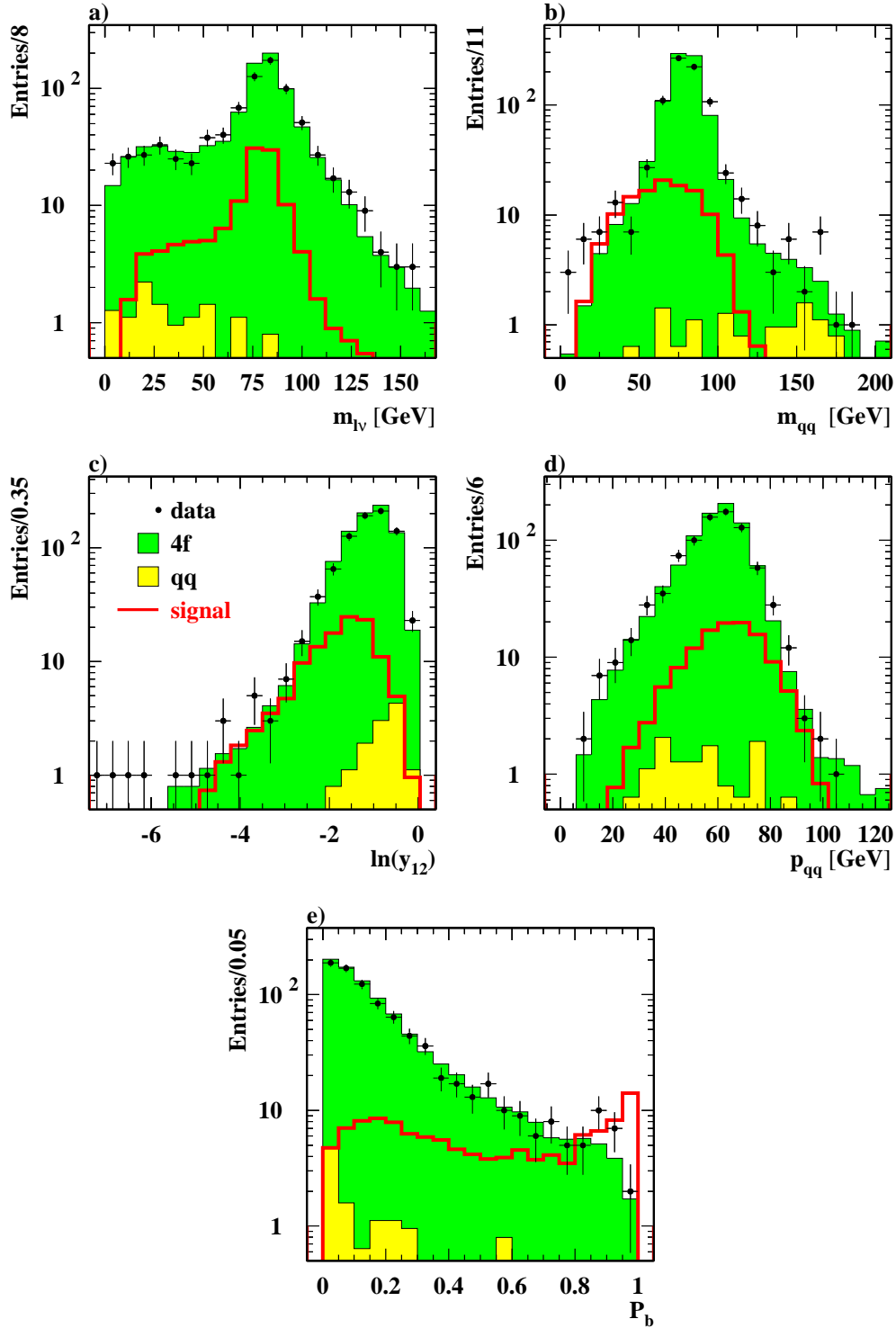


Figure 5.11: Likelihood variables at $\sqrt{s} = 206$ GeV: (a) reconstructed invariant mass of the W boson $m_{l\nu}$, (b) mass of the di-jet system m_{qq} , (c) jet resolution parameter $\ln y_{12}$, (d) momentum of the di-jet system p_{qq} and (e) b-tag probability P_b for the selected beauty jet.

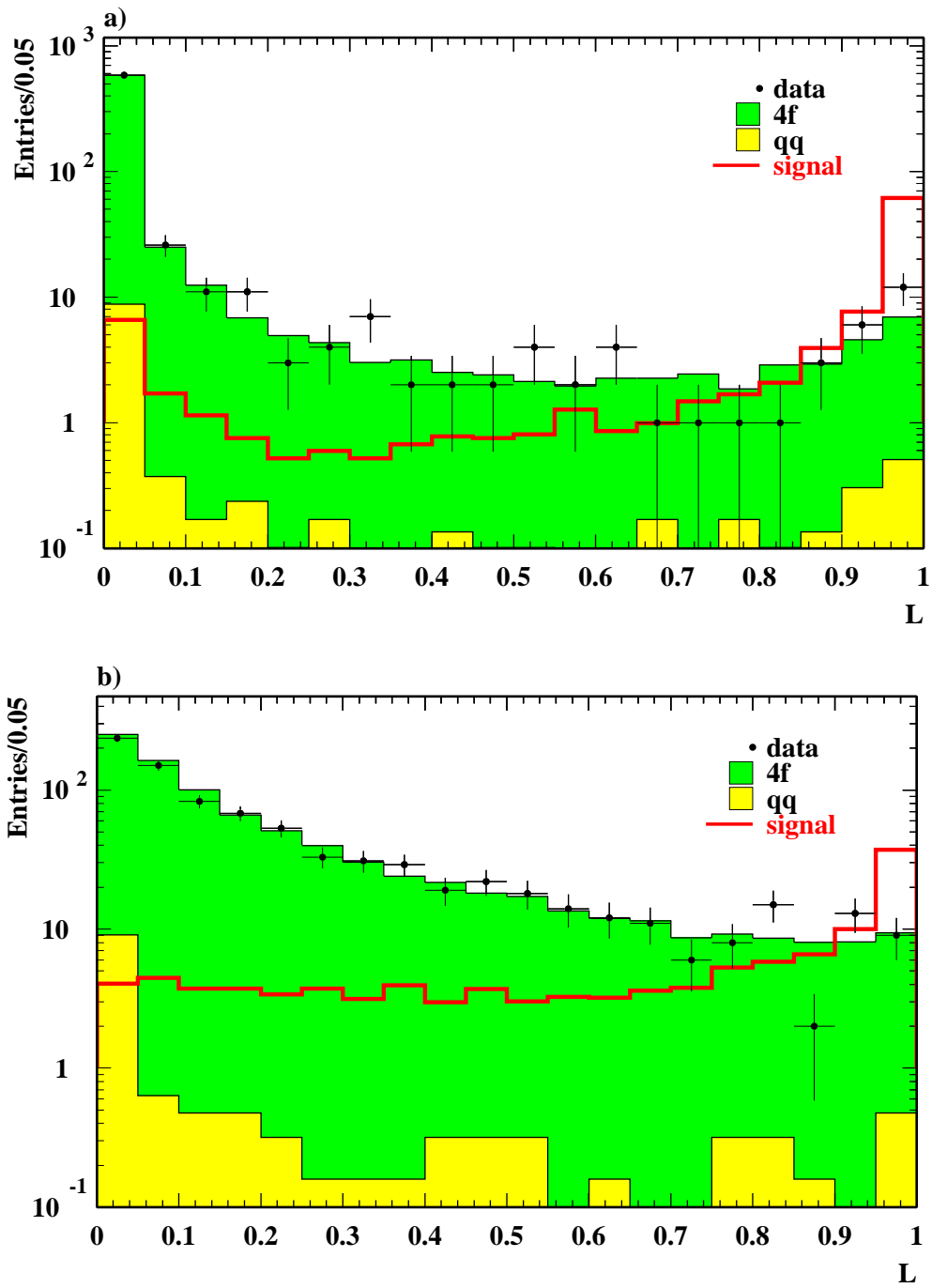


Figure 5.12: The Likelihood final discriminating variable for (a) $\sqrt{s} = 189$ GeV and (b) $\sqrt{s} = 206$ GeV center-of-mass energy.

The distribution of the final discriminating variable \mathbf{L} is shown in Figure 5.12 (a) and (b) for a center-of-mass energy of $\sqrt{s} = 189$ (206) GeV, respectively. The results for both data and Monte Carlo simulations are shown.

The distribution of \mathbf{L} shows a good agreement between data and SM background and a very good discriminating power between signal and SM background. The small peak of the distribution of \mathbf{L} near 0(1) for signal (background) events originates from small correlations between the variables which construct the final variable.

Due to the different kinematical characteristics at higher energies, the final discriminating variable has a different shape for $\sqrt{s} = 206$ GeV. The signal is kinematically not longer well separated from the WW background. Therefore the probability of a background event being classified as a signal event rises. As a result background events tend to have a value of \mathbf{L} higher than 0.

The signal expectations require an excess in the data to proof the single top quark production via FCNC. With respect to the background sources from SM expectations no excess is found in the data for both center-of-mass energies $\sqrt{s} = 189$ (206) GeV. The differences between data and SM background expectations are compatible with zero within statistical uncertainties.

Since the observed events doesn't show an indication of single top quark production via FCNC, an upper limit on the cross section σ_{stop} can be derived (in the next chapter). This is achieved by calculating an expected upper limit on the cross section for each value of the final discriminating variable \mathbf{L} .

Chapter 6

Results

A limit on the cross section for single-top quark production (σ_{stop}) via FCNC is derived and upper limits on the anomalous coupling constants are deduced and compared to the results received from other experiments.

6.1 Limit on the cross section

Based on Monte Carlo samples, an expected limit for σ_{stop} can be calculated. This is achieved by calculating first the expected number of signal events for the data reweighted with the Poisson probability for each value of the final discriminating variable \mathbf{L} . The result is then used to calculate the expected limit on the cross section taking into account the efficiency for each value of \mathbf{L} and the integrated luminosity for each center of mass energy. The distribution of the expected cross section is shown in Figure 6.1.

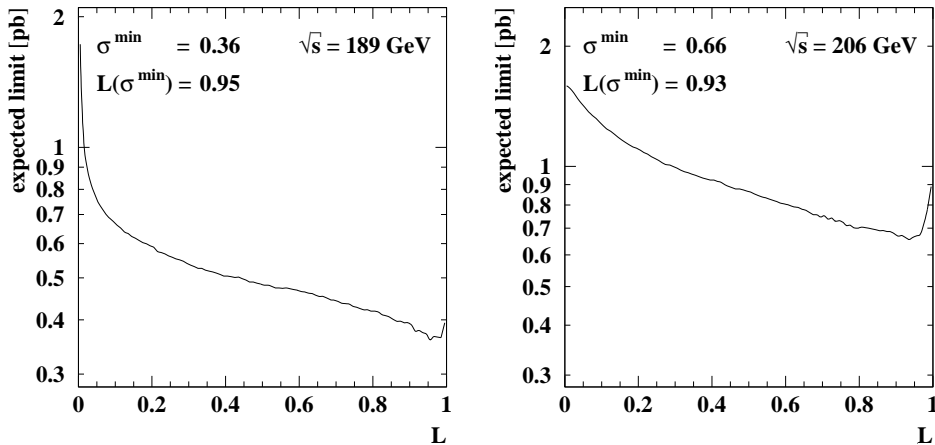


Figure 6.1: The expected limit for each value of \mathbf{L} at $\sqrt{s} = 189 \text{ GeV}$ and $\sqrt{s} = 206 \text{ GeV}$.

The optimal cut on the final discriminating variable in order to minimize the expected limit on the cross section is $\mathbf{L} > 0.95$ at $\sqrt{s} = 189 \text{ GeV}$ and $\mathbf{L} > 0.93$ at

$\sqrt{s} = 206$ GeV. These are the minimal values of the expected cross section taking into account the Poisson probability.

In total 13 candidates are selected in the data to be compared with 8.11 events in SM expectations for $\sqrt{s} = 189$ GeV. The cut on the final discriminating variable at $\sqrt{s} = 206$ GeV leaves 18 candidates in data to be compared with 14.5 in SM expectations (Table 6.1).

\sqrt{s} [GeV]	189	206
Luminosity [pb^{-1}]	172	211
Likelihood Cut \mathbf{L}	0.95	0.93
Number of Events in Data	13	18
Number of expected events in SM background	8.11	14.50
$\epsilon \cdot \text{BR}$ [%]	12.22	6.90
$\sigma_{\text{stop}}^{\text{expected}}$ (95% CL) [pb]	0.36	0.66
$\sigma_{\text{stop}}^{\text{observed}}$ (95% CL) [pb]	0.60	0.87

Table 6.1: The results after the cut on the final discriminating variable \mathbf{L} . The efficiency ϵ is multiplied by the SM branching fraction $\text{BR}(W \rightarrow l\nu \sim 33\%)$.

The efficiency for data collected at $\sqrt{s} = 206$ GeV is small due to larger value of energy from the charm jet: the signal is not longer kinematically well separated from the background especially the semi-leptonic WW background.

After this final cut the number of observed signal events at 95% confidence level (CL) is calculated by using

$$1 - \text{CL} = \frac{e^{\mu_B + N} \sum_{n=0}^{n_i} \frac{(\mu_B + N)^n}{n!}}{e^{\mu_B} \sum_{n=0}^{n_i} \frac{(\mu_B)^n}{n!}} =: 0.05 \quad (6.1)$$

where μ_B is the expected number of events in SM background, n_i is the number of selected events in the data and N is the maximum number of signal events. With the number N of signal events, the observed cross section σ_{stop} is calculated as follows

$$\sigma_{\text{stop}} = \frac{N/\epsilon}{\mathcal{L}} \quad (6.2)$$

where ϵ is the signal efficiency and \mathcal{L} is the integrated luminosity. The calculated upper limits for the expected and observed cross section σ_{stop} are shown in Table 6.1. The number of selected events in the data is higher than for the expected SM background. Therefore the observed limit is larger than the expected limit for both center-of-mass energies. These results were also verified with a cut-based analysis (Appendix A) and consistent results were found.

6.2 Uncertainties of the limit from the top quark mass

The largest uncertainty for the cross section σ_{stop} comes from the mass $m_t = 174.3 \pm 5.1$ GeV of the top quark given by the $D\theta$ and CDF experiments. To take into account the uncertainty of 5.1 GeV on the efficiency ϵ , Monte Carlo events for different masses of the top quark $m_t = 169, 179$ GeV are investigated (Table 6.2).

\sqrt{s} [GeV]	$m_{\text{top}} = 174$ GeV		$m_{\text{top}} = 169$ GeV		$m_{\text{top}} = 179$ GeV	
	ϵ [%]	$\sigma_{\text{stop}}^{\text{obs}}$ [pb]	ϵ [%]	$\sigma_{\text{stop}}^{\text{obs}}$ [pb]	ϵ [%]	$\sigma_{\text{stop}}^{\text{obs}}$ [pb]
189	12.22	0.60	10.31	0.61	12.10	0.71
206	6.90	0.87	5.60	1.07	7.82	0.77

Table 6.2: The upper limits (95% CL) on the cross section for different top masses.

The calculated upper limits for the cross section $\sigma_{\text{stop}}^{\text{obs}}$ show comparable efficiencies for the top mass of $m_t = 174$ GeV and $m_t = 179$ GeV. The obtained cross section is therefore not strongly dependent on the top quark mass. These results assume a 100% branching ratio for the top quark to decay $t \rightarrow bW$.

6.3 The limit for the anomalous coupling constants

A model-dependent upper estimate for the anomalous coupling constants k_γ and k_Z for the γ and Z exchange, respectively, is derived as described in section 2.4. The obtained limits for each center-of-mass energy are compared to the limits derived from CDF results and are shown in Figure 6.2.

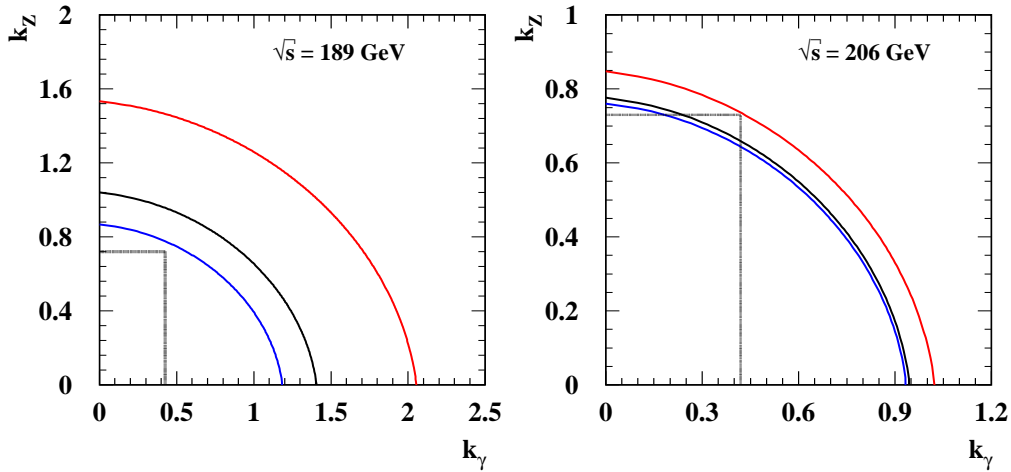


Figure 6.2: Model-dependent limits for $\sqrt{s} = 189$ (206) GeV. The black, blue (lowest) and red (upper) curved lines indicate the estimates on k_γ, k_Z for $m_t = 174, 169, 179$ GeV, respectively. CDF limits are indicated as black dashed lines.

The investigated process is sensitive for the anomalous coupling constant k_Z as the dominating contribution to the cross section comes from the Z boson exchange in the model described in section 2.4.

An upper estimate for k_Z is derived for the combined data. The limit is achieved by using the likelihood ratio method which has been developed for the search of the Higgs boson [38]. In this procedure the results for the different center-of-mass energies are weighted because the cross section strongly depends on them (Eq: (2.10)). The anomalous couplings in the mentioned model depend on the variation of the selection efficiencies (Table 6.2) and on the cross section for single top quark production as a function of the top quark mass. The combined limit for both center-of-mass energies is shown in Figure 6.3.

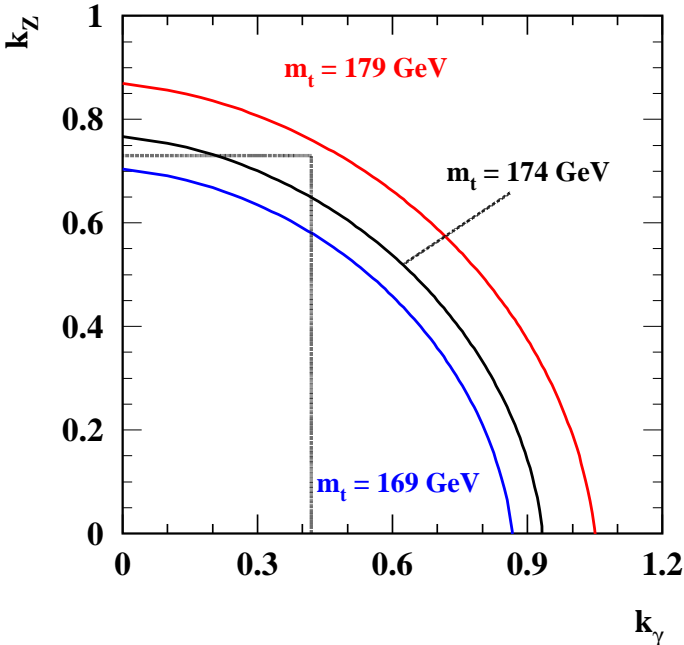


Figure 6.3: Model-dependent limits for the combined data. The black, blue (lowest) and red (upper) curved lines indicate the estimates on k_γ, k_Z for $m_t = 174, 169, 179$ GeV, respectively. CDF limits are indicated as black straight lines.

As the cross section is strongly dependent on the center-of-mass energy, the results obtained at higher energies are dominant in the resulting anomalous couplings. This leads to an upper limit of $k_Z < 0.77$ for a top quark mass of $m_t = 174$ GeV. For $m_t = 169(179)$ GeV the upper limits become $k_Z < 0.70(0.87)$. These results do not improve but are competitive to recent results given by other LEP experiments.

Chapter 7

Summary and Conclusions

In this thesis, the single top quark production via flavor changing neutral currents (FCNC) $Z \rightarrow t\bar{c}(\bar{u})$, ($Z \rightarrow \bar{t}c(u)$), has been investigated in e^+e^- collisions. The presented analysis focuses solely on the leptonic W boson decay $t \rightarrow bW \rightarrow b\ell\bar{\nu}$.

An integrated luminosity of 383 pb^{-1} of data was used, collected at center-of-mass energies of $\sqrt{s} = 189 \text{ GeV}$ and $\sqrt{s} = 206 \text{ GeV}$ by the OPAL detector at LEP.

As the FCNC is highly suppressed within the scope of the Standard Model, no events are expected to be found for the analyzed amount of data and any positive observation would be strong evidence for physics beyond the Standard Model.

The analysis is based on a likelihood method, where the constructed final discriminating variable has a value above 0.95 ($\sqrt{s} = 189 \text{ GeV}$) and 0.93 ($\sqrt{s} = 206 \text{ GeV}$) for selected signal events. The different cut at $\sqrt{s} = 206 \text{ GeV}$ results due to the minimization of the expected limit. A neural network has been used to identify events with an isolated lepton in the final state. Events which enter the likelihood method have to pass a set of preselection cuts. The dominating background arises from semi-leptonic WW events. Most of the background events from QCD, $\gamma\gamma$, ZZ and hadronic WW background are rejected.

At $\sqrt{s} = 189 \text{ GeV}$, 13 events were selected in the data to be compared with 8.11 events from the Standard Model expectations. At $\sqrt{s} = 206 \text{ GeV}$, 18 events were found in the data while 14.50 events are expected. The observed number of events in the data match with the expectations of the Standard Model background processes within their statistical errors and thus do not show evidence of single top quark production. Therefore model-independent upper limits at a confidence level of 95% on the single top quark production cross section σ_{stop} have been derived for both center-of-mass energies:

$$\begin{aligned} \sigma_{\text{stop}}^{\text{observed}} < 0.60 \text{ pb} \quad \sigma_{\text{stop}}^{\text{expected}} < 0.36 \text{ pb} \quad \text{at } \sqrt{s} = 189 \text{ GeV}, \\ \sigma_{\text{stop}}^{\text{observed}} < 0.87 \text{ pb} \quad \sigma_{\text{stop}}^{\text{expected}} < 0.66 \text{ pb} \quad \text{at } \sqrt{s} = 206 \text{ GeV}. \end{aligned}$$

The quoted limits assume a 100% branching ratio for the top quark decay $t \rightarrow Wb$ and a top quark mass of $m_t = 174 \text{ GeV}$. The top quark mass has an uncertainty of $\pm 5.1 \text{ GeV}$. Therefore the largest uncertainty for the cross section σ_{stop} comes from the top quark mass. This is taken into account for calculating the anomalous coupling constants. A model dependent upper estimate for the anomalous coupling constant k_Z

to the Z boson has been calculated for the combined data,

$$k_Z < 0.77 \text{ at } 95\% \text{ CL}$$

assuming $m_t = 174 \text{ GeV}$ and no anomalous coupling to the photon, $k_\gamma = 0$. This result is comparable to the constraints given by other LEP experiments. A combination of the leptonic and hadronic channel will improve the limit on k_Z and is accomplished in [39].

A combination of all LEP results will improve the limits derived from the CDF experiment at the Tevatron accelerator. Nevertheless no model for FCNC production can be excluded. In order to certain judge whether FCNC transitions occur in one of the mentioned models, searches at higher energies at the upgraded Tevatron and LHC must be performed.

Appendix A

Cut-based Study for Single Top Quark Production

A cut-based study for the leptonic channel is performed. The data and Monte Carlo samples described in Chapter 4 at $\sqrt{s} = 189$ GeV center-of-mass energy are used. The same global event selections and algorithms as in Chapter 5 apply.

The motivation for the cuts are the same as for the likelihood method. The cut-based method aims to reject all events with a different topology than the signal: two jets (one a high energetic beauty jet), an energetic isolated lepton and large missing transverse momentum. All applied cuts efficiently reduce the background and retain the signal. Following variables are used and the cuts applied successively in order of their appearance:

- (1) **NN-output** as in section 5.3.
- (2) $|\cos\theta_{\text{miss}}| < 0.9$ as in section 5.3.
- (3) $p_{\text{miss}} < 25$ GeV,
where p_{miss} is the missing momentum vector reconstructed from the visible momentum vector. This cut rejects events with no missing energy in the final state.
- (4) **1-C fit**,
where 1-C fit is a 1-constraint fit assuming H^+H^- or $W^+W^- \rightarrow qq\tau\nu$. The results for the Higgs events H^+H^- are equal 0, while the W^+W^- events reconstruct the decaying W. This cut rejects efficiently WW semi-leptonic events.
- (5) $60 \text{ GeV} < m_{l\nu_1} < 100 \text{ GeV}$,
where $m_{l\nu}$ is reconstructed as in section 5.4. This cut rejects a large portion of the semi-leptonic WW background.
- (6) $\ln(y_{12}) < -1.6$,
where $\ln(y_{12})$ calculated as in section 5.4. This cut rejects semi-leptonic WW events efficiently.
- (7) $m_{qq} < 75$ GeV,
where m_{qq} is calculated as in section 5.4. This cut reduces the WW background.

- (8) $P_b > 0.3$,
 where P_b is calculated as in section 5.4. After this final cut, only 4 events are left in the data.

All distributions are shown in the following plots. The 4f background is indicated in green, the qq background in yellow and the signal as a red line.

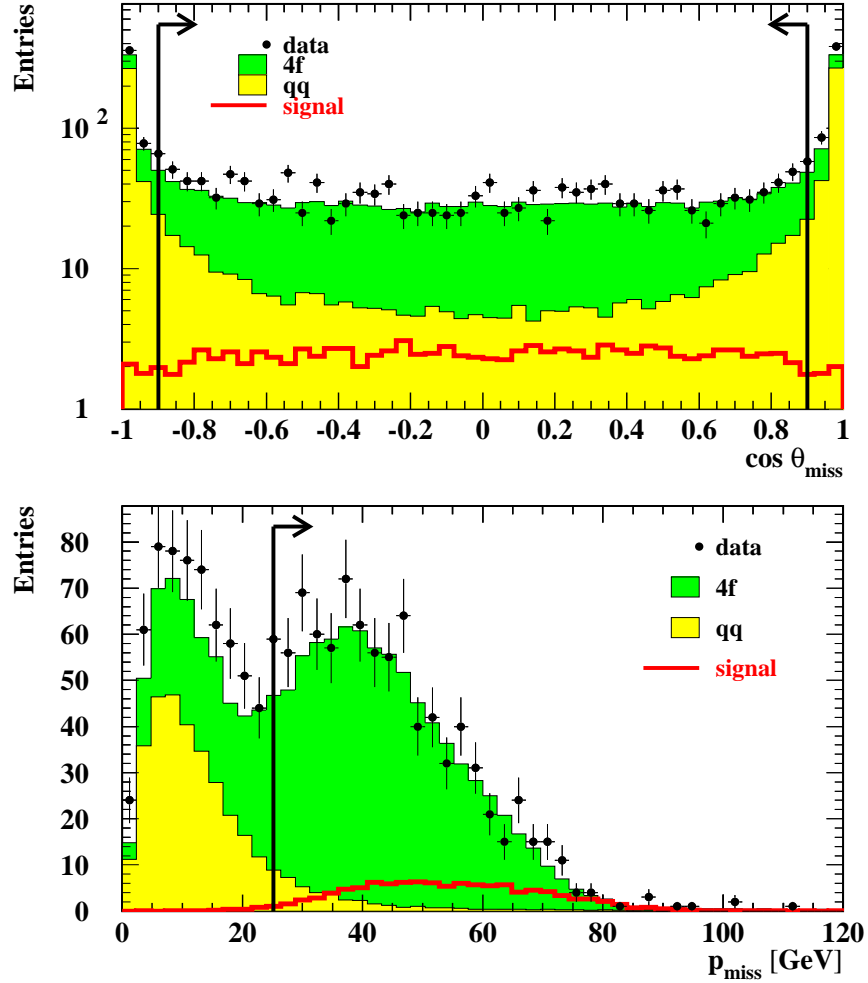


Figure A.1: Cut-based study: the upper plot shows the distribution of the angular momentum from the missing momentum $\cos\theta_{\text{miss}}$, the lower plot shows the distribution of the missing momentum p_{miss} ; all previous cuts are applied.

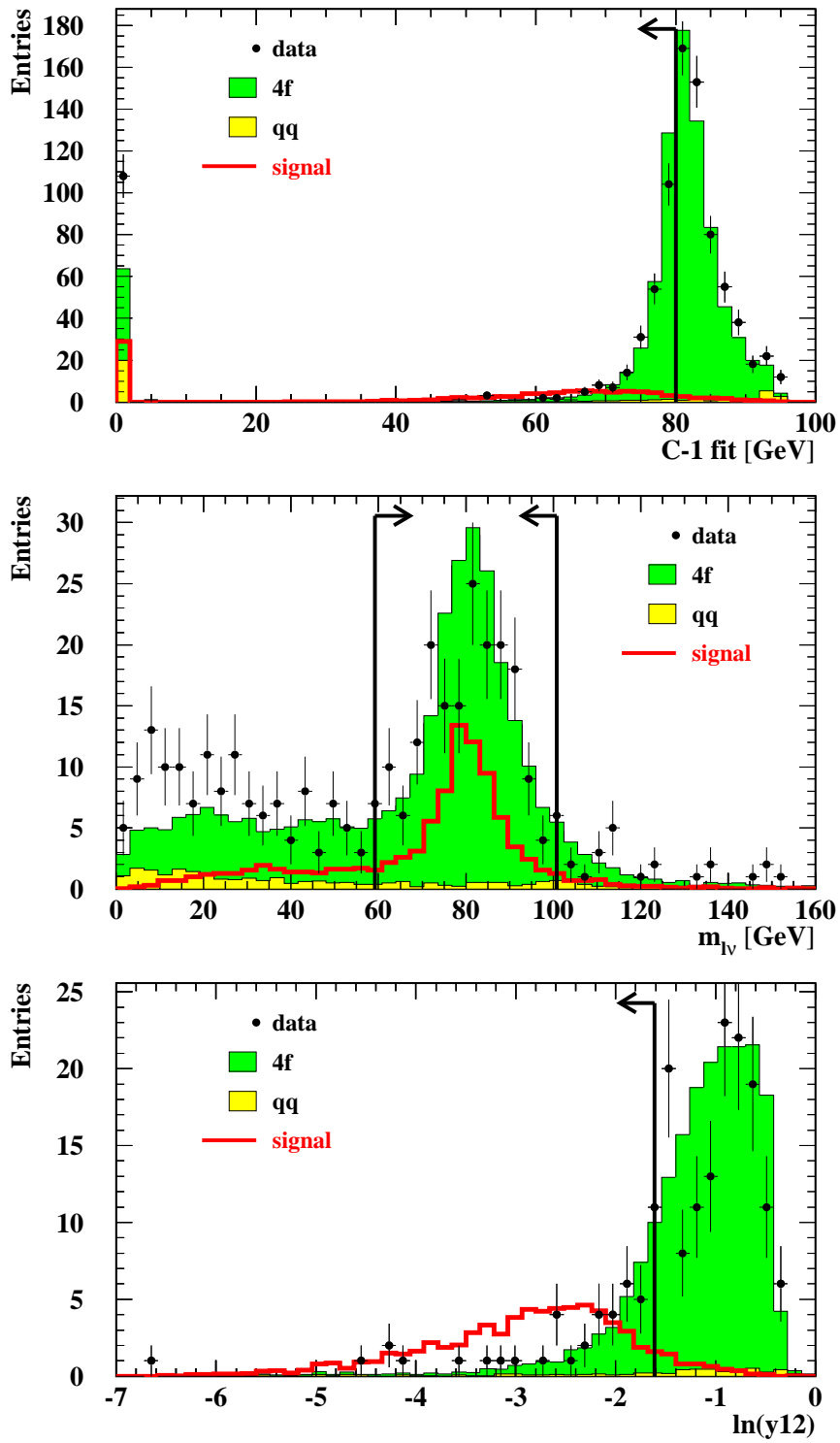


Figure A.2: Cut-based study: the upper plot shows the 1-C fit , the middle plot the distribution of the reconstructed W boson mass $m_{l\nu}$ and the lower plot the jet resolution parameter $\ln(y_{12})$; all previous cuts are applied.

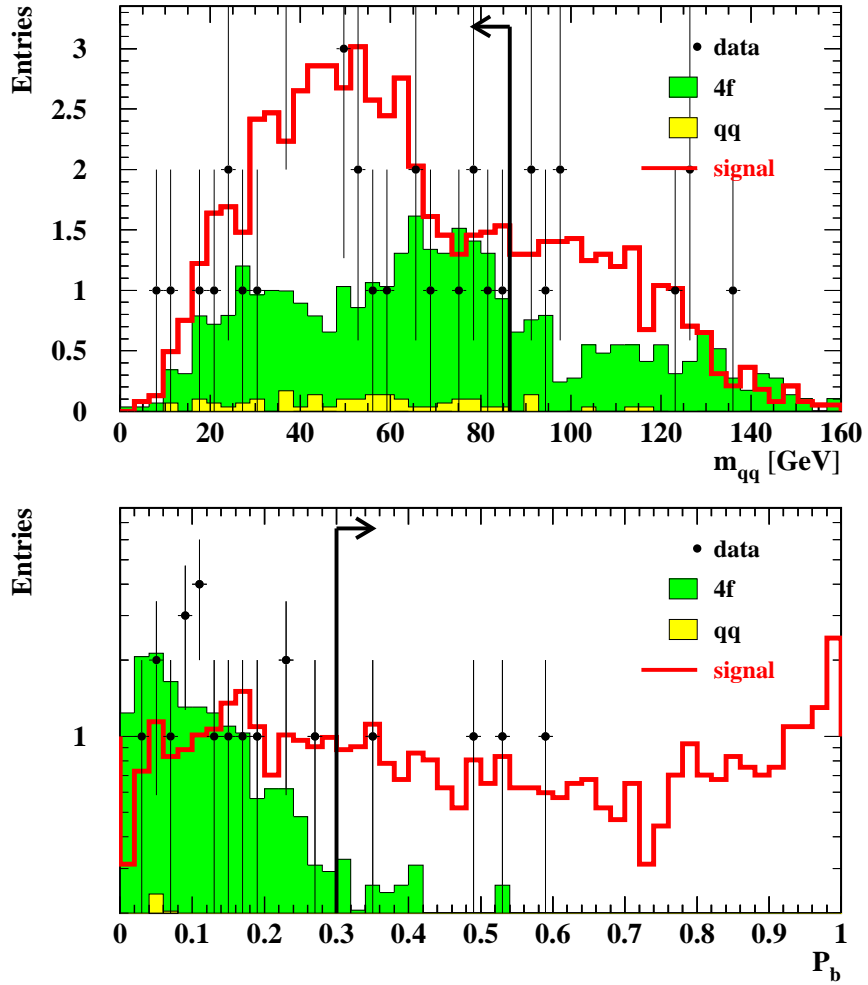


Figure A.3: Cut-based study: the upper plot shows the distribution of the mass from the di-jet system m_{qq} , the lower plot shows the b-tag probability; all previous cuts are applied.

The cut-flow table for the applied cuts is shown in the lower table. The 4f background is negligible, the qq background is efficiently reduced. The dominating background arises from the semi-leptonic WW background.

cut	data	All Bgd	llqq	q \bar{q}	4f	$\epsilon \cdot \text{BR} \%$
no cut	18177	17132.2	1404.8	13927.7	1799.7	29.6
NN-output	2498	2235.6	976.3	983.2	276.0	23.1
$ \cos\theta_{\text{miss}} < 0.9$	1526	1372.1	886.5	337.7	147.9	21.3
$p_{\text{miss}} < 25 \text{ GeV}$	884	829.1	775.7	40.7	12.6	20.8
1-C fit	343	318.6	281.8	27.2	9.6	18.7
$60 < m_{l\nu} < 100$	180	194.2	187.4	5.6	1.2	13.6
$\ln(y_{12}) < -1.6$	38	34.2	32.0	2.0	0.2	12.5
$m_{\text{qq}} < 75 \text{ GeV}$	22	19.7	18.0	1.6	0.1	8.1
$P_b > 0.3$	4	3.8	3.4	0.4	0.0	5.3

After all cuts are applied, 4 events are left in the data to be compared to 3.8 events expected from the SM background. The expected background and the data are in a good agreement. No excess is observed. Therefore a limit on the cross section is derived as described in chapter 6.

$\sqrt{s} \text{ [GeV]}$	189
Luminosity [pb^{-1}]	172
Number of Events in Data	4
Number of expected events in SM background	3.8
$\epsilon \cdot \text{BR} \text{ [%]}$	5.3
$\sigma_{\text{stop}}^{\text{observed}} \text{ (95\% CL) [pb]}$	0.66
$\sigma_{\text{stop}}^{\text{expected}} \text{ (95\% CL) [pb]}$	0.66

Table A.1: Cut-based study: The upper limits on the cross section for single top quark production in the leptonic channel.

The efficiency ϵ is multiplied by the SM branching fraction $\text{BR}(W \rightarrow l\nu \sim 33\%)$. These results assume a 100% branching ratio for the top quark to decay $t \rightarrow bW$.

Bibliography

- [1] CDF Collaboration (F. Abe et al.). *Phys.Rev.Lett.*, 73:225, 1994.
- [2] D. Atwood et al. *Phys. Rev.*, D(53):1199, 1996.
- [3] N. Cabibbo. *Phys. Rev. Lett.*, 10:531, 1963.
- [4] S.L. Glashow et al. *Phys. Rev.*, D(2):1285, 1970.
- [5] D.E. Groom et al. *Eur. Phys. J.*, C(15):1, 2000.
- [6] S.L. Glashow. *Nucl. Phys.*, 20:579, 1961.
- [7] S. Weinberg. *Phys. Rev. Lett.*, 19:1264, 1967.
- [8] A. Salam. in *Elementary Particle Theory*, ed. N. Svartholm (Almqvist and Wiksells, Stockholm, 1968).
- [9] D. Griffiths. *Einführung in die Elementarteilchenphysik*. Akad. Verl., Berlin, 1996.
- [10] B. Povh et al. *Teilchen und Kerne*. Springer Verl., Berlin, 5., korr. und erw. aufl. edition, 1999.
- [11] H. Fritzsch. *Phys. Lett.*, B244(number 4):423, 1989.
- [12] C-S. Huang et al. *Phys.Lett.*, B(452):143, 1999.
- [13] K. Hagiwara et al. *Phys.Lett.*, B(325):521, 1994.
- [14] H. Fritzsch, D. Holtmannspötter. *Phys. Lett.*, B(457):186, 1999.
- [15] G. Eilam et al. *Phys. Rev.*, D(44):1473, 1991.
- [16] J.L. Lopez et al. *Phys. Rev.*, D(56):3100, 1997.
- [17] V.F. Obraztsov et al. *Phys. Lett.*, B(426):393, 1998.
- [18] CDF Collaboration (F. Abe et al.). *Phys.Rev.Lett.*, 80:2525, 1998.
- [19] S. Willenbrock. *hep-ph/0103033*, 2000.
- [20] OPAL Collaboration (K. Ahmet et al.). *Nucl.Instrum.Meth.*, A(305):275, 1991.

- [21] W. Blum and L. Rolandi. *Particle Detection with Drift Chambers*. Springer Verlag, 1993.
- [22] F. Sauli. CERN 77-09, 1977.
- [23] J. Allison et al. *Nucl.Instr.Meth.*, A(317):47, 1992.
- [24] OPAL Collaboration, G. Alexander et al. *Z. Phys.*, C(69):543, 1996.
- [25] T. Sjöstrand. *Comp. Phys. Comm.*, 82:74, 1994.
- [26] J. Fujimoto et al. *Comp. Phys. Comm.*, 100:128, 1997.
- [27] R. Engel and J. Ranft. *Phys. Rev.*, D:4244, 1996.
- [28] S.L. Lloyd. The OPAL Primer. Technical Report Version 98a, July 1998.
- [29] S. Yamashita et al. TN 575, OPAL, Nov 3rd 1998.
- [30] OPAL Collaboration (M.Z. Akrawy). *Phys.Lett.*, B(253, number 3,4):511, 1991.
- [31] D. Glenzinski, A. Hocker. TN 559, OPAL, August 7 1998.
- [32] S. Catani et al. *Phys.Lett.*, B(269):432, 1991.
- [33] N.Brown et al. *Phys. Lett.*, B(252):657, 1990.
- [34] OPAL Collaboration, G. Abbiendi et al. *Eur. Phys. J.*, C(7):407, 1999.
- [35] S. Yamashita. TN 578, OPAL, Nov 3rd 1998.
- [36] D. Karlen. *Comp. in Phys.*, 12(4):380, 1998.
- [37] D. Karlen. *Comp. in Phys.*, 12:4:380, 1998.
- [38] T. Junk. *Nucl. Inst. and Meth.*, A(434):435, 1999.
- [39] OPAL Collaboration. 2001. unpublished.

Acknowledgements

I'd like to thank everybody who participated in this research for

Single Top Quark Production via Flavor Changing Neutral Current

starting with:

- Ms. Prof. Dr. Dorothee Schaile, who encouraged me to take up this challenge in the research for new physics
- Dr. Thomas Trefzger, who taught me how to deal with all the information I got and supervised this thesis till the very last moment
- Axel Leins, who taught me a lot about computing and search algorithms and how to find the limit for the cross section, as he never believed when I told him I found the single top (he was proved to be right)
- Sofia Chouridou who improved my English a lot; without her perfect English teaching I would not have plucked up the courage to write the thesis in English
- Dr. Jörg Dubbert, who showed me how to display two pages in one using ghost-view, Johannes Elmsheuser, who corrected this thesis twice for perfect English, Dr. Oliver Sahr, who accompanied me on my birthday to CERN
- Dr. Madjid Boutemour and Dr. Raimund Ströhmer with whom I had fruitful conversations about physics, Patricia Mendez, who gave me her Teddy bear in the most stressful time I had
- all my experimental physicists for elementary particles colleagues in Munich and all members from the 'Rechnergruppe'
- all my friends who cheered me up and who called this thesis the top-single-beautiful-charming thing.

Ich danke meinen Eltern die mich immer unterstützt haben und mir das Studium der Physik ermöglicht haben.

Finally I'd like to explain what thank you means for me:

**'Thank you!' means you don't have to
but I'm glad you did.**

'Danke!' heisst Du müsstest nicht
aber ich freue mich dass Du es getan hast.

Erklärung

Ich erkläre hiermit, die vorliegende Arbeit selbständig verfasst zu haben und keine anderen als die angegebenen Quellen und Hilfsmittel verwendet zu haben.

München, den 30. April 2001

Meta Binder